Republic of Iraq
Ministry of Higher Education &
Scientific Research
Al Muthanna University
College of Science
Department of Physics

Modeling In-Line Mach-Zehnder Optical Microfiber For Sensing Applications

A Thesis Submitted in Partial Fulfillment of the

Requirements for the Degree of Master in Physics Science

BY

Hanan Jasim Mohammed

B.Sc. 2003

Supervisors

Assist. Prof. Dr. Firas Faeq K. Hussain   **Assist. Prof. Dr. Muwafaq F. Jaddoa**

2021 A.D   **1443 A.H**

بِسْمِ اللَّهِ الرَّحْمَنِ الرَّحِيمِ

"اللَّهُ نُورُ السَّمَاوَاتِ وَالأَرْضِ مَثَلُ نُورِهِ كَمِشْكَاةٍ فِيهَا
مِصْبَاحٌ الْمِصْبَاحُ فِي زُجَاجَةٍ الزُّجَاجَةُ كَأَنَّهَا كَوْكَبٌ
دُرِّيٌّ يُوقَدُ مِن شَجَرَةٍ مُّبَارَكَةٍ زَيْتُونَةٍ لّا شَرْقِيَّةٍ وَلا
غَرْبِيَّةٍ يَكَادُ زَيْتُهَا يُضِيءُ وَلَوْ لَمْ تَمْسَسْهُ نَارٌ نُّورٌ عَلَى
نُورٍ يَهْدِي اللَّهُ لِنُورِهِ مَن يَشَاء وَيَضْرِبُ اللَّهُ الأَمْثَالَ
لِلنَّاسِ وَاللَّهُ بِكُلِّ شَيْءٍ عَلِيمٌ"

صدق الله العلي العظيم

سورة النور الآية 35

Certification

We certify that this thesis entitled "***Modeling In-Line Mach-Zehnder Optical Microfiber For Sensing Applications***" was prepared by "***Hanan Jasim Mohammed*** " under our supervision at the Department of Physics, College of Science, Al Muthanna University as a part of the requirements of the Master degree of Science in Physics.

Supervisor	**Supervisor**
Assist. Prof. Dr. Firas Faeq K. Hussain	**Assist. Prof. Dr. Muwafaq F. Jaddoa**
Date :	**Date:**

Recommendation of the Head of Physics Department

In view of the available recommendations, we forward this thesis for debate by the examining committee

Dr. Salah A.H. Al Murshidy

Head of the Department

Date:

ACKNOWLEDGEMENT

Thanks for God's blessing and for the holy Prophet Mohammed bin Abdullah peace be upon him. First of all, I would like to thank Allah, the most merciful for helping me during my study.

I would like to express my special appreciation and thank my supervisors, Assist. Prof. Dr. Firas Faeq K. Hussain and Assist. Prof. Muwafaq F. Jaddoa for their supervision and for providing me valuable necessary observation and assistance in this work, who haven't been mere supervisors, may Allah grant them all goodness.

My acknowledgment for College of Science, Physics Department / Al Muthanna University, for giving me access to the institution to complete the research. I am thrilled to present my nephew Eng. Ayah U. Witwit special thanks for her support and encouragement.

I am very much thankful to my husband and my children for their love, understanding, prayers and continuing support to complete this research work.

Hanan J. Mohammed

Dedication

To the one who honored me by bearing his name

My father, may God have mercy on him …

To the one who gave the most precious things

A her prayers and words which were companions of brilliance and excellence

My mother … in order to reach this degree

but she gone before she saw it

To my dear brothers and sisters

With all my love ...to the companion of my way

My dear husband

To my joy in life … my children

Hanan J. Mohammed

Abstract

Waveguide-based electro-optic modulators are widely employed in the field of optical communication, optical signal processing, and optical sensors, owing to the rapid development of photonic integrated circuits. As a type of optical switching element, the Mach-Zehnder modulator is one of the most extensively used device structures, with the advantages of high accuracy and sensitivity. Through theoretical and numerical analysis, three types of Mach-Zehnder modulator based on ferroelectric materials which are lithium niobate ($LiNbO_3$), Peroviskite and potassium nitrate have been studied. The transmission characteristics of each type of Mach-Zehnder modulator are numerically analyzed while an electric field is applied across one arm of waveguide. Mach-Zehnder modulator (MZM) based ferroelectric materials has been studied theoretically and simulated by using finite element method with COMSOL Multiphysics software. Different parameters of MZM have been experimented which are coupling length, bending radius and applied voltage. The results has showed that the lowest coupling length of MZM is 304 μm by using KNO_3 crystal. MZM operates as a modulator at bend radius of curvature with 2.5mm for all three ferroelectric crystals and MZM didn't work with lower than this radius. The effect of utilized voltage has shown that MZM operates actively at 0.38 V by using $SriTO_3$. While for $LiNbO_3$ and KNO_3, the effective voltages are 0.45V and 0.5V, respectively. The power loss for all MZM samples is 2%.

Table of Contents

List of Figures

List of Tables

List of Symbols

Sample	Definitions
SMF	Single-mode fiber
MZI	Mach-Zehnder Interferometers
ns	Surrounding medium
n_1	Refractive index of the first medium
n_2	Refractive index of the second medium
EW	An evanescent wave
FEWS	Evanescent-wave spectroscopy
TIR	Total-internal-reflection
IR	In farad spectrum
FTIR	Fourier-transform
Θ_C	The critical angle
(M/C)	Monitor and control circuits
T_C	Curie temperature
EOM	Electro-optic modulator
NLO	Nonlinear optical
2D	Two Dimension
IO	Integrated optical
Si	Silicon
MOS	Metal-oxide-semiconductor
MZM	Mach-Zehnder modulator
V	Voltage
R	Resistance
FEM	Finite element method
PDEs	Partial differential equations
EM	Electro magnetic
Θ	The angle of incidence

TIRF	Total internal reflection fluorescence
ATR	Attenuated total reflection
X	Function of position
t	Time
E	Electric field
D	Electric displacement
B	Magnetic Induction
H	Magnetic field
J	Current density
μ_o	Permeability of light in vacuum
ε_o	Permittivity of Vacuum
J_d	Displacement current
TE	Transmission of electric field
TM	Transmission of magnetic field
TEM	Transmission of electric and magnetic field
σ	Sigma: the surface charge
E_1	Envelope function
k	Wave vector
r	The position
β	The propagation constant for the mode
neff	The effective index of the waveguide mode
k_o	The vacuum wave number
α	Is the angle from the x-axis
$LiNbO_3$	Lithium niobate
$SrTiO_3$	Perovskite (strontium titanium oxide)
KNO_3	Potassium nitrate
µm	Micrometer (µm)
d-dc	Distance- directional coupler

Chapter one

Introduction

1.1 Introduction

The early of 1970s saw some of the first experiments on low-loss optical fibers being used, not for telecommunications, as had been the prime motivation for their development in the 1960s, but for sensor purposes [1]. Waves that are guided Nonlinear optics represented a fast-paced and dynamic study subject that has yielded a slew of intriguing – if not fascinating – results in recent years. Simultaneously, it is making rapid progress from the optical laboratory to a variety of devices in industries ranging from telecommunications to biosciences. It's not a new field of study, but one with a long history dating back to the early days of low-loss waveguides. Because of the combination of height intensities, lengthy interaction lengths, and control of the propagation constants, optical fibers and waveguides provide unique and different conditions for nonlinear optics. They are also becoming increasingly technologically significant. The subject has a lengthy history, but it continues to evolve quickly, most recently with the introduction of new types of optical fiber [2].

1.2 Optical Fiber and Waveguide

The core, cladding, and coating or buffer are the three components of an optical fiber. Figure (1.1) depicts the basic structure. The core is a dielectric cylindrical rod, which is usually constructed of glass. The fiber's core is where light propagates the most. A dielectric substance with a high index of refraction serves as the cladding layer. The cladding material has a lower index of refraction than the core material. Typically, the cladding is made of glass or plastic. The cladding serves a variety of purposes, including reducing light loss from the core into the surrounding air, reducing scattering loss at the core's surface, protecting the fiber from surface impurities, and increasing mechanical strength [3].

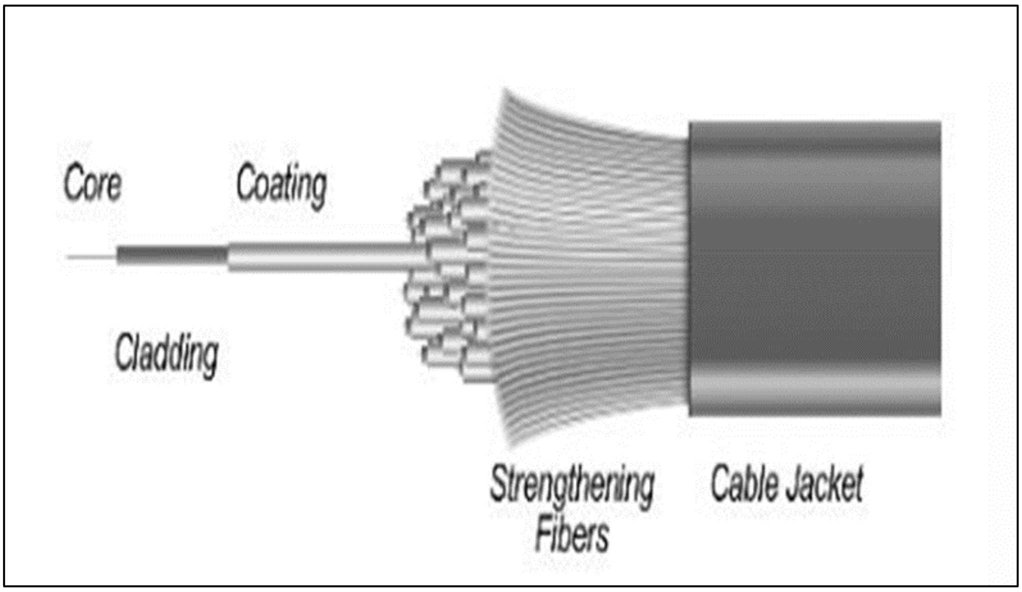

Figure (1.1): Basic structure of an optical fiber [2].

Recently, the optical community has shown a very high demand for novel material platforms for the development of different areas of photonics. The optical waveguides produced using this technology represent a new platform to study novel optical materials that could not be explored differently as this fabrication process does not require etching of the core material itself [4]. Since its invention in the early 1970s, the use of and demand for optical fiber have grown tremendously. The uses of optical fiber today are quite numerous. With the explosion of information traffic due to the internet, electronic commerce, computer networks, multimedia, voice, data, and video, the need for a transmission medium with the bandwidth capabilities for handling such vast amounts of information is paramount. Fiber optics, with its comparatively finite bandwidth, has proven to be the solution [5]. The laser 1960 and the current low-loss optical fiber are two of the most major technical discoveries that led to the development of current optical fiber sensors. Both have their roots in prior decades' work on the maser, the microwave ancestor of the laser, and the short-length lowtransparency fibers employed in early endoscopes for medical and industrial uses. This pioneering work quickly led to the formation of a number of research groups devoted to the application of this new technology in sensing and measurement. Since then, the field has continued to advance and develop tremendously [6].

Optical waveguide devices already have played important roles in telecommunications systems, and their importance will certainly grow in the future. People considering which computer programs to use when designing optical waveguide devices have two choices: develop their own or use those available on the market. A thorough understanding of optical waveguide analysis is, of course, indispensable if they are to develop our own program [7]. To connect the laser couple source in the MZI we need to used Single-mode fiber (SMF). Immunological effects or biomarkers are detected in the sensor arm while the reference arm include liquid with similar refractive index of sensing arm, to reduce the common mode noise caused by mechanical and temperature fluctuation. The oriented mode in the sensing arm expertise a phase shift, $\Delta\varphi$ and thus, when the changing of effective index .when the splitting of optical waveguide into two arms, after a certain distance they are recombined again. The length(L) is opened in sensor arm, for making the waveguide come in connect with surrounding environment, an protective layer is used to avoid the interference in the interferometer. when a light is passing through the sensor arm ,shifting of the phase is induced, which leads to change the optical properties of the surrounding medium [8]. In recent years, fiber optic sensors have been developed from the laboratory research and development stage to practical applications. The market for fiber optic sensor technology may be divided into two broad categories of sensors: intrinsic and extrinsic. Intrinsic sensors are used in medicine, defense, and aerospace applications, and they can be used to measure temperature, pressure, humidity, acceleration, and strain. Extrinsic sensors are used in telecommunications to monitor the status and performance of the optical fibers within a network [9]. In an optical fiber, if the refractive index of the surrounding medium (ns) is less than the core refractive index (n_1) then the power in the fiber core is insensitive to the environ- mental changes in the surroundings. On the other hand, if (<5), then the power in the core decreases exponentially (ns $\approx$ n_1) and the fiber cladding is only of few wavelengths and will penetrate into the surroundings However, in fibers where the refractive indexes are not equal, an evanescent wave (EW) effect is still experienced with a penetration depth of the order of wavelength [10].

Fiber-optic evanescent-wave spectroscopy (FEWS) has been a prominent analytical approach for IR absorbance spectroscopy over the last ten years. FEWS uses IR transparent optical fibers as sensing elements and is based on the attenuated total-internal-reflection TIR phenomenon. Fast, real-time, in-situ, selective, nondestructive, and safe detection are all advantages of this technology. It has been used to study solid–liquid interfaces, chemical reaction rates, complicated material curing, organometallic thin films, liquid and gas detection and monitoring, centration measurements, and biological applications in a variety of configurations. Normally, the sensing elements are housed in a Fourier-transform IR (FTIR) spectrometer system, although tunable lasers have lately been used in FEWS systems in place of blackbody sources. The method's wave-length resolution, sensitivity, and detection limit have all increased as a result of this [11].

1.3 Ferroelectricity

Ferroelectricity is a property of certain nonconducting crystals, or dielectrics, that exhibit spontaneous electric polarization that may be reversed in direction using an electric field. All ferroelectric crystals are pyroelectric and piezoelectric by definition. A ferroelectric material exhibits spontaneous polarization in the absence of an electric field and can be switched in direction by applying an electric field. Ferroelectric materials have electrical properties similar to ferromagnetic materials [12]. Ferroelectric materials are characterized by a permanent electric dipole that can be reversed through the application of an external voltage, but a strong intrinsic coupling between polarization and deformation also causes all ferroelectrics to be piezoelectric, leading to applications in sensors and high-displacement actuators [13]. A spontaneous polarization can be altered periodically by an electric field in a homogenous ferroelectric single crystal [14]. The surface chemistry of ferroelectrics with a fixed polarization state has been explored experimentally. The ferroelectric spontaneous polarization can not only improve the charge separation and transfer in the bulk, but also promote the surface charge separation of photocatalysts by forming a heterojunction between a photocatalyst and ferroelectric our group disclosed the influence of ferroelectric spontaneous polarization on surface charge migration behavior [15].

1.4 Mach – Zehnder in Optical Fiber

The Mach–Zehnder interferometer is a device used to determine the relative phase shift variations between two collimated beams derived by splitting light from a single source. The interferometer has been used, among other things, to measure phase shifts between the two beams caused by a sample or a change in length of one of the paths.

The apparatus is named after the physicists Ludwig Mach (the son of Ernst Mach) and Ludwig Zehnder, there are many types of MZI like grating, loop, line [16].To address this requirement, a variety of optical fiber-based sensing approaches have been developed. Due to its resilience to electromagnetic interference, compact size, possible low cost, and ability to distribute measurement across a large distance, optical fiber sensors can be exceptionally useful and adaptable devices. High sensitivity, a high degree of integration, design simplicity, and compactness are all advantages of fiber Mach-Zehnder interferometers (MZIs). A number of optical fiber refract meters have recently been reported that can measure refractive index and several other parameters at the same time. These optical fiber sensors work as evanescent wave sensors that use multimode interference schemes to monitor changes in the environment's optical properties. They use the dependence of high-order mode propagation constants on the refractive index of the surrounding medium to monitor changes in the environment's optical properties. Only a few RI ranges are often considered in studies reporting refractive index measurement utilizing fiber MZI devices. Because of their useful characteristics, such as small size, high-resolution detection, excellent aging characteristics, ability to operate in chemically hazardous environments, and immunity to electromagnetic noise, fiber optic refractive index (RI) sensors have gotten a lot of attention in the last few years for chemical and biochemical monitoring applications. Many studies have attempted to improve the usefulness of optical fiber RI sensors by increasing sensitivity, improving resolution, simplifying fabrication procedures, lowering cost, improving sensor structure robustness, and lowering insertion loss, and because of their useful characteristics، such as small size, high-resolution detection, excellent aging characteristics, ability to operate in chemically hazardous environments, and immunity to electromagnetic noise.

Many researchers have tried to enhance the effectiveness of optical fiber RI sensors by improving sensitivity , enhancing resolution, simplifying fabrication techniques , dropping cost, increasing the robustness of sensor structure , and reducing insertion loss [17]. For incidence angles greater than the "critical angle," a light beam propagating through a transparent medium with a high index of refraction (e.g. a solid glass prism) encounters an interface with a medium with a lower index of refraction (e.g. an aqueous solution) undergoes total internal reflection. The critical angle θc is equal to $\sin^{-1}$ (n2/n1), where n2 and n1 are the liquid and solid refractive indices, respectively. Despite the fact that the incident light beam completely internalizes at the interface, an electromagnetic field known as a "evanescent wave" penetrates the liquid medium for a short distance and propagates parallel to the surface in the plane of incidence [18]. Although there are several different types of Si modulator, they all suffer from the thermal drift problem and, consequently, realizing efficient monitor and control circuits (M/C) that can provide reliable operation for Si modulators is very important. Furthermore, with the perspective for future photonic and electronic monolithic integration, such M/C circuits should be easily integrated with other photonic devices with minimal power consumption and chip area [19]. The laser source is coupled into the MZI via single-mode fiber (SMF). To improve coupling efficiency, a mode-size converter is utilized to match the mode size of the input SMF and the waveguide of the MZI. The guided mode is separated into two branches at the Y-branch splitter: sensing arm and reference arm. The sensing arm detects immunoreactions or biomarkers, while the reference arm contains liquid with a refractive index equal to that of the sensor arm to minimize common mode noise produced by mechanical and temperature fluctuations. Due to the cladding index change produced by immunoreactions, guided mode at the sensing arm undergoes phase shift, and hence effective index change, Neff respect to the reference arm [20]. Broadband electro-optic intensity modulators are essential to convert electrical signals to the optical domain very low nonlinear distortions, simultaneously. However, a modulator with all those characteristics has not been demonstrated [21].

1.5 Literature Review

In 2004 George T. Paloczi, Yanyi Huang, and Amnon Yariv, studied the Mach–Zehnder electro-optic polymer amplitude modulator is fabricated by a simple and high-throughput soft-stamp replica-molding technique. The modulator structure incorporates the highly nonlinear and stable chromophore, AJL8, doped in amorphous polycarbonate. Single-arm phase-retardation results in a halfwave voltage sVpd of 8.4 V at 1600 nm. The on/off extinction ratiois better than 19 dB, resulting from precise Y-branch power splitters and good waveguide uniformity. These results indicate that the simple fabrication process allows for good optical performance from high-fidelity replicas of the original master device [22].

In 2005 P K Shukla*, K K Sarangpani, S Talwar, G S Purbia, S V Nakhe, H S Vora, investigating a theoretical model has been established, and they reveals that the linearity can be improved by properly adjusting the RF power, the bias voltage, and the operation point of the primary and the secondary MZMs. The measurement results show the IMD can be suppressed by about 9.9 dB m, while the fundamental tones only reduced by 1.1 dB m at 10 GHz for the dual-parallel MZM compared to the primary MZM only. This results in a 2.9 dB improvement in SFDRIMD. A larger Pp /Ps can be obtained by incorporating a VOA into the slave MZM so that the third-order harmonic can be further suppressed to give a lower IMD [23].

In 2006 Tsung-Hsin Lee,1 Fu-Tsai Hwang,1 Wen-Tron Shay,2 and Ching-Ting Lee3 used the electromagnetic field sensor using a $LiNbO_3$ Mach-Zehnder optical modulator and an antenna has been developed to measure the electromagnetic field. This sensor operated at a wavelength of m, for which many fiber optical systems have been developed. The minimum detectable filed intensity of this electromagnetic field sensor is 0.7 mV/m at 50 MHz and 1.2 mV/m at 3 GHz respectively. The sensitivity was relatively flat from 50 MHz to 3 GHz and this frequency range uniquely covers all frequency bands involved in the cellular phones, mobile communication, and Bluetooth technology. According to the experimental results, this electromagnetic field sensor so developed can be potentially employed in sensory applications on electromagnetic compatibility and RF and microwave safety control [24].

In 2007 Hitoshi Kiuchi, Tetsuya Kawanishi, Senior Member, IEEE, Masumi Yamada, Takahide Sakamoto, Member, IEEE, studied the high carrier suppression optical double-sideband intensity modulation technique using the integrated $LiNbO_3$ MZ modulator, which is capable of compensating the imbalance of the MZ arms with a pair of active trimmers (null-bias operation mode). The full-bias point operation mode introduced in this paper is also a novel modulation technique for the second-order harmonic generation. The MZ modulator can generate two coherent lightwaves with frequency difference equivalent to four times the modulation frequency. Photonic local signals of 120 GHz can also be generated using this technique. The phase stability over 100 GHz could not be measured due to the reduction of the multiplier power; however, estimated phase stability and coherence loss indicate that this method is applicable to ALMA and VLBI experiments [25].

In 2008 Mona Jarrahi, Thomas H. Lee, and David A. B. Miller used the MZ modulators for RF photonics are required to have low modulator driving voltages to allow for realistic circuit sizes, and sufficient bandwidth to operate at desired microwave frequencies. In this work, they have designed and fabricated a GaAs–AlGaAs MZ modulator, which achieves low drive voltage by utilizing QCSE-induced refractive index change along a relatively long modulator length and a high-speed modulation speed by employing a traveling-wave modulation scheme to relax the efficiency-bandwidth tradeoff. They obtained an extremely low driving voltage of 0.45 V for a signal-electrode of 1.5 mm at 870-nm wavelength. The measurement-instrument-limited small signal modulation bandwidth is measured to be 18 GHz, projected to an estimated bandwidth of 50 GHz. To our knowledge, this is the lowest reported MZ modulator driving voltage at such high modulation bandwidths Monolithically integrated photodetectors found in the same structure show an impulse response time of 8-ps FWHM, and saturation power of 330 mW [26].

In 2009 Morozov, Oleg, Aybatov, Dmitry used the device for conversion of single frequency signal into two-frequency signal, based on lithium niobate dual-drive Mach-Zehnder modulator was proposed. Symmetrical two-frequency MZM output signal was obtained, when applied modulation signals were equal but inversed $\nu1(t) = - \nu2(t)$. Operation points for modulation signals at MZM transfer function were chosen at positive and negative slopes at the quadrature point $V+$ bias $= - U\pi/2$ and $V-$ bias $= U\pi/2$. That also allowed to remove the phase modulation (chirp) of the output signal. Numerical simulation for cases when modulation signals had different phase were held, spectrum evolution of output signal was considered [27].

In 2010 Michael R. Watts, William A. Zortman, Student Member, IEEE, Douglas C. Trotter, Ralph W. Young, and Anthony L. Lentine have developed a silicon depletion mode phase modulator that maximizes the overlap of the depletion region with the optical mode enabling a π phase shift with only 5 V applied to be achieved in a ~2-mm-long structure, thus realizing a VπL of only ~1 V•cm. Further, in a 500- μm-long lumped element device, they demonstrate a 10-Gb/s NRZ data transmission with wide-open complementary output eye diagrams and without the use of signal preemphasis. The measured 3-dB electrical bandwidth of the modulator was measured to be ~8 GHz, limited only by the RC time constant of the 50-Ω transmission-line-driven lumped element. Future improvements, such as the inclusion of traveling wave electrodes and more aggressive doping schemes, will likely enable even higher bandwidth (>40 GHz) operation with even lower VπL figures of merit [28].

In 2011 Yuan Yu, Jianji Dong, Xiang Li, and Xinliang Zhang studied Positive and negative monocycle pulses are generated when the MZM is biased at the positive and the negative slopes of the modulation curve, respectively. Both the RF spectra of generated polarity-reversed monocycle pulses comply with the FCC definition very well. The influences of the injection current of SOA, the bias voltage of MZM, the carrier wavelength and the pulse width on the monocycle pulse and the RF spectrum are experimentally studied. Experimental results show that the bias voltage of MZM, the bias current of SOA and pulse width of electrical signal can affect the generated monocycle pulse distinctively, but the influences of the optical carrier wavelength on monocycle pulse is tolerable, and the scheme can be implemented in the whole C-band. The symmetry of both the positive and negative monocycle pulses can be improved by increasing the bias current of SOA. Due to the character of fast depletion and slow recovery of the carrier in SOA, the pulse width of the positive monocycle pulse is wider than that of the negative monocycle pulse, leading to a narrower RF spectrum [29].

In 2012 Wei Li, Ning Hua Zhu, Member, IEEE, and Li Xian Wang studied in DPMZM, two sub-MZMs were biased at minimum and maximum transmission points, respectively, to generate a CS-DSB+OC modulated signal. In this way, a phase-shift between the CS-DSB and OC signals was generated by controlling the dc bias of MZM3. This tunable phase-shift leads to an adjustable power-fading function, resulting in a tunable ACF. As a result, the IFM system is reconfigurable with tunable measurement range and resolution. In principle, the measurement range can be tuned to any frequencies, which is only limited by the bandwidth of the optical transmitter and receiver employed [30].

In 2013 Robert Palmer, Luca Alloatti, Dietmar Korn, Philipp Claudius Schindler, Moritz Baier, Jens Bolten, Thorsten Wahlbrink, Michael Waldow, Raluca Dinu, Wolfgang Freude, Christian Koos, and Juerg Leuthold have demonstrated a 1.5 mm long push-pull silicon organic hybrid MZI modulator with a $V\pi$ of 1.8 V at DC and 2.5 V at a data rate of 10 Gbit/s, which corresponds to apolymer nonlinearity of $r33 = 15$ pm/V. Open eye diagrams and an extinction ratio of (4–11) dB are demonstrated for drive voltages as low as 800 mVpp making electrical RFamplifiers dispensable. Improvements are possible concerning the poling procedure. With a fully poled structure the limit for $V\pi$ would be around 390 mV for this Mach–Zehnder structure and the chosen nonlinear polymer. The result forecasts ultralow energy consuming electro-optic interconnects with silicon modulators directly driven by on-chip CMOS digital-to-analog converters [31].

In 2014 Wei Li, Member, IEEE, Wen Ting Wang, and Ning Hua Zhu, Member, IEEE have demonstrated a photonic RF waveform generator based on a DPMZM driven by a sinusoidal RF signal. The desired RF waveform can be generated by separately controlling the powers of the even- and odd-order sidebands, the power ratio between the even- (or odd-) order sidebands, and the power/phase of the optical carrier. As a result, it is possible for us to manipulate the powers of the RF harmonics after photo detecting by the PD. In this way, the desired RF waveforms can be generated. In order to generate high-speed RF waveforms, modulator and PD with higher bandwidths are required. Moreover, they can only control the power of the RF harmonics up to the third-order one. Thus, only the approximation of the desired waveform can be achieved, which reduces the flexibility of the proposed method to generate arbitrary waveforms [32].

In 2015 W. Talataisong,1,2 D. N. Wang,1,3,* R. Chitaree,2 C. R. Liao,1,4 and C. Wang1 In conclusion, the fiber in-line MZI has been proposed and demonstrated for pressure measurement. The gas pressure variation induces the RI change in the air-cavity, which causes the change in optical path difference of the MZI, and in turn leads to the transmission spectrum shift The proposed device is miniature in size, robust in structure, and stable in operation and exhibits a high pressure sensitivity of ~8239 pm/MPa. This project is supported by the National Natural Science Foundation of China (Grant No. 61377094) and the Hong Kong government general research fund (GRF) grant PolyU 152163/14E. One of authors would like to acknowledge the Development and Promotion of Science and Technology Talents Project (DPST) of Thailand for the student scholarship [33].

In 2016 Eduardo Huerta-Mascotte 1 Juan M. Sierra-Hernandez 2,*, Ruth I. Mata-Chavez 1 Daniel Jauregui-Vazquez 2 , Arturo Castillo-Guzman have proposed and demonstrated a new Mach –Zhnder interferometer based on a non -zero dispersion shifted fiber. Here, the MZI was implemented by a core offset splicing of a NZ-DSF between segments of SMF, and several fringe contrast of 2.25, 4.27, 5.22 and 20.54 dB were obtained respectively. Moreover, the MZI was tested behavior due to the shearing stress that is not uniform at the core-offset MZI structure. Here, by experimental measurements, they determined a sensitivity of 0.070 nm to a physical length of the NZ-DSF of 2.5 cm [34].

In 2017 Muwafaq F. Jaddoa studied the characteristics of an IMMZI were investigated by observing the change in the FSR as the waist diameter was decreased from 10μm to 13μm in 1 μm steps. Moreover, these four samples were utilized as RI sensors for NaCl solutions with different concentrations. The RI values of the NaCl solutions ranged from 1.31837 to 1.31928 RIU. It was concluded that the IMMZI sample with the smallest diameter (10 μm) compared with the other samples had the highest sensitivity of 2913.7 nm/RIU as a result of the increase in the evanescent field strength with a decreasing OMF diameter [35].

In 2018 Shinsuke Tanaka , Takasi Simoyama, Tsuyoshi Aoki investigated a low-power-consumption Si photonics PAM4 transmitter. Using a simple fabrication process, an efficient PIN-PS was integrated with a RC filter. It exhibited a low $V\pi L$ of 0.19 Vcm. The Si photonics chip with the PIN+RC phase shifter was flipchip bonded with an energy efficient 28nm CMOS inverter driver. The segmented MZ modulator was designed for 56 G bps PAM4 operation by changing the equalizer capacitance CE and the inverter size between MSB and LSB segment. The fabricated transmitter exhibited clear PAM4 output waveforms up to 56 Gbps. It demonstrated a record-high energy efficiency of 1.59 mW/Gbps among Si PAM4 transmitters. They also confirmed that the PAM4 waveform exhibit lower BER than FEC limit up to 50 Gbps even with an un-equalized receiver [36].

In 2019 TATSUROU HIRAKI, 1,2,* TAKUMA AIHARA demonstrated a high-efficiency MZM on a Si platform using a 300-μm-long membrane InP-based phase shifters and low-loss deuterated SiN waveguides. The small VπL of 0.4 Vcm was achieved with the insertion loss of 4.5 dB by optimizing the overlap between the distributed carriers and optical mode field. In addition, the fabricated device showed error free operation for 40-Gbit/s NRZ signal. These results shows that the proposed device has the potential to further reduce the cost, size, and power consumption of optical transceivers [37].

In 2020 Yiwei Xie 1,2, Ming Zhang 1,2 and Daoxin Dai 1,2,* have presented a novel design rule for achieving an MZI sensor with ultra-high sensitivity. For any given optical waveguide system, they have shown that tunable sensitivity can be achieved for an MZI sensor by choosing the MZI arm lengths appropriately. An example has been given with SOI nanowires, and the device sensitivity can be as high as 106 nm/RIU (or higher). With such an MZI sensor, it is possible to detect a very tiny refractive index change as small as 10−6 RIU, even by using an OSA with a low resolution of ~1 nm. This is really helpful because a moderate/low-resolution OSA can be available for the measurement of the spectral responses. In particular, it is even possible to integrate with an on-chop spectrometer, which usually has a relatively low resolution. In this way it becomes very attractive for realizing a low-cost optical sensing system [38].

In 2021 Youngseok Bae * , Sunghoon Jang , Sungjun Yoo , Minwoo Yi , Joonhyung Ryoo and Jinwoo Shin A digital video broadcasting application has been investigated with the modulation formats such as QAM (Quadrature Amplitude Modulation) and PSK (Phase Shift Keying) under the three optical mediums like OWC, FSO and LOS-FSO. The transmitter and the receiver sections of a Digital Video Broadcasting unit have been designed using QAM and PSK. These two sections have been analyzed completely and the parameters of quality factor and the Bit Error Rate are attained using the optisystem and optispice software. The LASER driver circuit is designed in optispice whereas the communication blocks are designed using optisystem and both were co-simulated. The input driver has been simulated for four different wavelengths of 850 nm, 1064 nm, 1330 nm and 1550 nm. The distances analyzed is 2 km. A 10gbps bandwidth has been utilized for the simulation of optical communication mediums. On the comparative simulated results of the QAM and PSK modulation formats with the three optical channels OWC, FSO and LOS-FSO, it is concluded that the PSK performs well with OWC and LOS-FSO; whereas the FSO performs well with QAM modulation format. From the performance analysis, it is implicated that the system with the best Q-factor is achieved at the wavelength of 1064 nm [39].

1.6 Aims of Study

The aims of this study are to obtain the relations of:

1) The power difference and coupling length.
2) Total transmission and bend radius.
3) Transmission and applied voltage.

Chapter Two

Principles of Optical Modulator and Ferroelectric Materials

2.1 Introduction

Nonlinear fiber optics has continued to grow during the decade of1990s، perhaps even more dramatically than anticipated. This growth is motivated by several recent advances in light wave technology, the most important is the advent of high-capacity fiber-optic communication systems. In such systems, the transmitted signal is amplified periodically by using optical amplifiers to compensate to residual fiber losses. As a result, the nonlinear effects accumulate over long distances, and the effective interaction length can exceed thousands of kilometers! Among other fiber devices in which nonlinear effects are becoming increasingly important, are mode-locked fiber lasers, distributed fiber amplifiers. The response of any dielectric to light become nonlinear for intense electromagnetic fields. In the transparent region of optical fiber The intensity dependence of the refractive index leads to a large number of interesting nonlinear effects [2].

2.2 Modulators

Optical modulation is one of the most crucial operations in photonics. It is ubiquitous in photonics and optoelectronics applications, such as optical interconnect environmental monitoring, bio sensing, medicine and security applications. Optical modulators can be categorized in different ways. For example, depending on the attribute of light that is modulated (panel a), optical modulators can be classified into amplitude modulators, phase modulators, polarization modulators, wavelength modulators and so on. Depending on the principle of operation (panel b), optical modulators can be classified into [40] :

2.2.1 Electro-Optic Modulator

An electro-optic modulator (EOM) is an optical device in which a signal-controlled element exhibiting an electro-optic effect which is used to modulate a beam of light. The modulation may be imposed on the phase, frequency, amplitude, or polarization of the beam. Modulation bandwidths extending into the gigahertz range are possible with the use of laser-controlled modulators, electro-optical modulator in compact silicon structures. The modulator is based on a resonant light-confining structure that enhances the sensitivity of light to small changes in refractive index and also enables high-speed operation, Electro-optic modulators represent one of the most critical components in optoelectronic integration, and decreasing their size may enable novel chip architectures [41].

2.2.2 Thermo-Optic Modulator

Thermo-optic modulators have been realized in near-IR (NIR) silicon components , and although they exhibit much smaller modulation bandwidths than plasma dispersion effect modulators, they have been shown to be compactable , require low power , and are much simpler to fabricate [42]. Practically, thermo-optic modulator could be a more feasible solution considering the large thermo-optic coefficient (1.86 × 10-4 K-1) in silicon and intensive researches in the last decades, It is noteworthy that the thermal conductivity of grapheme is as high as 5300 W (mK)-1 , 30 which is ~100 times higher than that of gallium aesnide,31 indicating an excellent capability of transferring heat at a high speed. It has been reported that graphene can induce a fast temperature variation of about 100 °C when injected by 12 m W electrical power[43].

2.2.3 Magneto-Optic Modulator

The development of devices based on superconducting qubits for quantum information processing has been advanced dramatically in the recent years. However, two issues stand in the way of superconducting qubits' widespread use: the inability to send quantum states over long distances and the lack of a long-term memory. These two issues have created a new subject called "hybrid quantum systems," which looks into the coupling of superconducting qubits to a variety of different physical systems like spin systems and nano-mechanical systems. The two challenges could alternatively be overcomed by using reversible inter-conversion between microwave photons (which naturally link to superconducting qubits) and optical photons, as well as optical fibers for long-distance quantum state transmission [44]. A magnetic-sensitive medium exhibits circular birefringence, difference in the refractive indices for left- and right-handed circular polarization, by applying a magnetic field. This is known as the Faraday Effect. Thus, when two counter-rotating circularly polarized pulses propagate through a medium [45] .

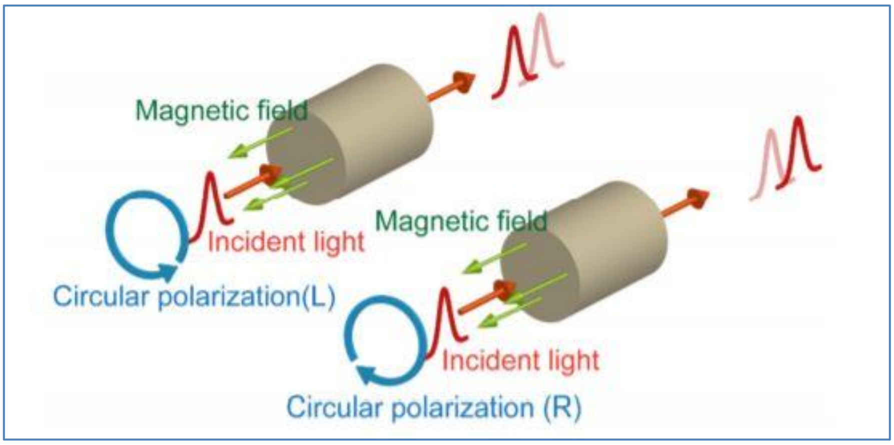

Figure (2.1): Sketch of the magneto-optic effect as a pulse with circular polarization travels through a magnetic-sensitive medium. A clique delay is induce with a magnetic field[45].

2.2.4 Acousto–Optic Modulator

For a long time, acousto-optic effects have been exploited for optical modulation, with Bragg cells being the most well known example. However, in future generations of integrated photonics, the desire for quick and compact devices, as well as needed phase matching, imposes various limits on standard acousto-optic devices. As a result, a promising approach to increasing operation speed employs all-optical light control, which allows operation down to sub picosecond time scales; these devices are typically a few hundreds of μms long because they rely on optical nonlinearities,they are frequently little Photonic crystals (PhCs) are an excellent way to reduce device size. Thermo-optical switches based on a PhC Mach-Zehnder interferometer MZI with 12m-long arms on an AlGaAs/GaAs system3 and electro-optical switches based on carrier injection of an 80m-long silicon PhC-MZI are examples. Using the nonlinear features of quantum dots inserted in the MZI arms, faster PhC-based all-optical switching devices have been accomplished in the Al,GaAs system. Fabrication of PhC. On the other hand, necessitates a sophisticated process with extremely tight tolerances [46]. And so on, depending on the optical property of the material changed for light modulation.

2.2.5 All-optical modulators

All-optical light modulation using 2D layered materials has been extensively studied as it allows the signal processing to be realized fully in the photonic domain. Thus, modulation can be done directly in an optical fiber or other waveguide (for example, silicon waveguide) system, allowing ultrafast, low-loss and broadband optical signal processing in simple configurations. Demonstrated all-optical modulators with 2D materials include saturable absorbers ،wavelength convertors, optical limiters and polarization controllers. The majority of these devices exploit the strong nonlinear optical response of 2D materials ,their broad bandwidth, fast response and miniature size for compact[40].

2.3 Mach –Zehnder modulator

An optical interconnection link using a Mach-Zehnder modulator (MZM) is common and well researched. In the area of electrical modeling, most of these modulators are treated as transmission lines [47]. A fiber optic MZM interferometer is one of the basic configuration used in high-sensitivity measurements [48]. Integrated optical (IO) devices are capable of combining high sensitivity, mechanical stability, miniaturization and possibility of mass production. That is the reason why they have a wide application .Optical Mach-Zehnder interferometer (IO-MZI) poses distinct advantages. Firstly, sensitivity of IO-MZI can be further improved by increasing the interaction length (L) regardless of the sensitivity limit of waveguide. Secondly, IO-MZI offers a readily available reference arm to reduce the thermal, temperature and mechanical noise which is crucial to improve the detection limit of all biosensor. Next, output response of IO-MZI is based on direct intensity detection instead of wavelength shift [8]. Since advanced optical modulation formats have received considerable interest over the last few years, we want to point the reader to some additional reviews on the topic, supplementing the material presented here Direct modulation of lasers is the easiest way to imprint data on an optical carrier. Here, the transmit data is modulated onto the laser drive current, which then switches on and off the light emerging from the laser [49]. Due to its resilience to electromagnetic interference, compact size, possible low cost, and ability to distribute measurement across a large distance, optical fiber sensors can be exceptionally useful and adaptable devices. High sensitivity is particularly advantageous for fiber Mach-Zehnder interferometers (MZIs). To address this requirement, a variety of optical fiber-based sensing approaches have been developed [50]. Fiber optic tapers are crucial sensors and couplers that can be used in a variety of applications. The majority of tapers are based on single mode fiber optics.A Mach-Zehnder phase modulator, based on an interferometric configuration, which converts phase modulation into intensity modulation. The phase of the optical beam traveling through a first arm of the interferometer is altered relative to the phase in the second arm by applying an appropriate modulating voltage to an electrode associated with the first arm. In one such configuration, the modulating voltage is applied to each arm in an equal [51].For optical measurements, the driver is wire-bonded to a depletion-mode Mach-Zehnder modulator. A distributed driver architecture significantly increases the bandwidth for the large voltage stress [52] . It is challenging to achieve high speed optical intensity modulation in silicon (Si) because the material does not exhibit any appreciable electro-optic effect ,the design based on the free-carrier plasma dispersion effect wherein the phase shifting elements of a Mach Zehnder interferometer (MZI) are metal-oxide-semiconductor (MOS) capacitors embedded in Si rib waveguides. An applied voltage induces an accumulation of charges near the gate dielectric of the capacitor, which, in turn, modify the refractive index profile of the waveguide and ultimately the optical phase of light passing through it. The MOS capacitor operates exclusively in accumulation bias so that the device bandwidth is not limited by carrier recombination in Si [53].

2.4 Structure of Mach –Zehnder Modulator (MZM)

The structure of Mach –Zehnder (MZM) modulator as shown in figure (2.2).MZMs work by the principle of interference, controlled by modulating the optical phase, the power of the input is splited equally into the two output waveguides of the first directional coupler. Those two waveguides form the two arms of a Mach-Zehnder interferometer, by applying on one of the arms of an electric field to modify the refractive index in the material and, thus, modify the phase for the wave propagating through that arm. The two waves are then combined into another 50/50 directional coupler. By changing the applied voltage ,you can continuously control the amount of light exiting from the two output waveguides [54].

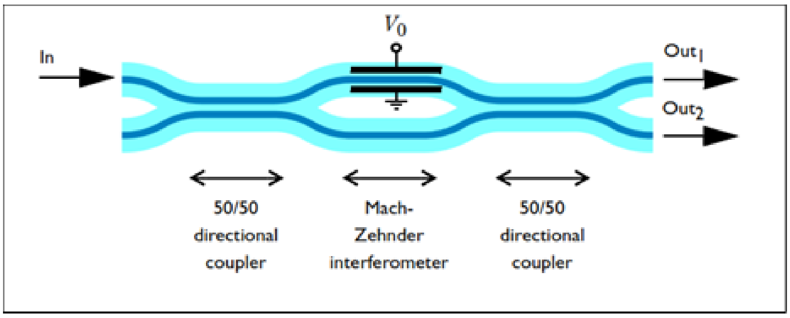

Figure (2.2): Structure of Mach –Zehnder modulator[54]

Optical modulators are used for electrically controlling the output amplitude or the phase of the light wave passing through the device. To reduce the device size and the driving voltage, waveguide-based modulators are used for communication applications. To control the optical properties with an external electric signal, the electro-optic effect, or Pockels effect, is used, where the birefringence of the crystal changes proportionally to the applied electric field. A refractive index change results in a change of the phase of the wave passing through the crystal. If you combine two waves with different phase change, you can interferometrically get an amplitude modulation [55].

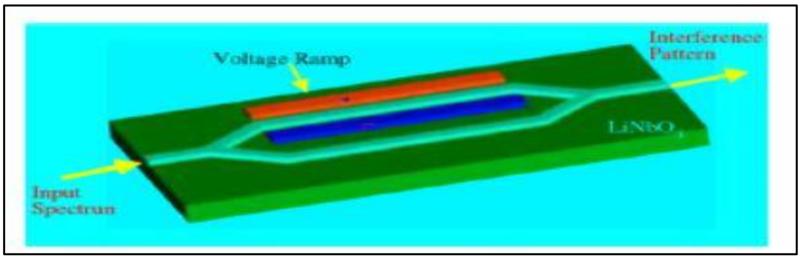

Figure (2.3): Integrated Mach-Zehnder micro-interferometer on $LiNbO_3$ [55].

MZMs, especially $LiNbO_3$-based devices, as shown in figure (2.3) feature wavelength are independent modulation characteristics, excellent extinction performance (typically 20 dB), and lower insertion losses (typically 5 dB) than EAMs. The required (high-speed) peak-to-peak drive voltages of up to 6 V. However, ask for broadband driver amplifiers, which can be challenging to build at data rates in excess of 10 Gb/s.Today,$LiNbO_3$-based MZMs which are widely available for modulation up to 40 Gb/s[49]. On a modified Mach-Zehnder interferometer which is capable of measuring the ultra short time strain response of a sample. Using this instrument, the dispersion of piezoelectric and electrostrictive coefficients of several commonly used ferroelectrics were examined [56]. Mach–Zehnder interferometers (MZIs) on SOI platform are used as optical switches, filters, modulators and sensors, as they show large thermo-optic effect, high optical index difference, low propagation and coupling losses. prompted by the demand of ultra-fast and more compact switching, sensing and modulating devices for telecommunication and iter- net industry, and for sensing applications . The accompanying challenges include finding ways to further reducing power consumption ,and minimizing power losses [57]. The numerical effects of several parameters on absorption sensitivity are investigated. The taper core is not in direct touch with the external medium due to the cladding, resulting in some substantial changes from the uncladded one, especially when the external medium index approaches the index of cladding or core. To demonstrate the possibility of such a chemical sensor, tapers are made and absorption experiments are carried out. Fiber optic tapers are crucial sensors and couplers that can be used in a variety of applications. The complete wave theory is used to model most tapers, which are based on single mode fiber optics. The theory is based on the fact that light waves driven through a fiber have a power portion in the form of evanescent waves in the cladding.[58]. Glass optical fiber waveguides with low loss were first produced between the late 1960s and the early 1970s, (Ka70), and were immediately developed together with other necessary and related optical components to be used the communication is industry , advanced technological development continues apace, spurred by applications of fiber optic systems in telecommunications, computing and process control . From around 1977, this rapidly maturing technology has been applied to the intensive development of sensing devices (Gi82, Cu84, Bu85, Pi85, Da88, Ar89, Cu89a, Ud91). The most advanced work has been done on rotation detectors, or gyroscopes and on acoustic field sensors have also been developed to detect physical quantities such as strain and displacement, pressure, temperature, acceleration, magnetic field, electric current and electric field.[59] Optical fiber sensors have attracted great attentions in the applications of biological, chemical and environmental industries, including the measurements of the liquid level, refractive index (RI), temperature and strain. Compared to the other techniques that based on the mechanical and electrical methods, the optical fiber sensors have many advantages, such as electromagnetic immunity, resistance to erosion, high sensitivity and capability of remote sensing. In the past years, several types of fiber optical sensors have been developed. For example, the sensors based on the long period fiber gratings Recently, sensors based on all-fiber Mach-Zehnder interferometer (MZI) have received considerable attention [60].Due to its resilience to electromagnetic interference, compact size, possible low cost, and ability to distribute measurement across a large distance, optical fiber sensors can be exceptionally useful and adaptable devices. These optical fiber devices operate as evanescent wave sensors based on multimode interference schemes, exploiting the dependence of high-order mode propagation constants on the refractive index of the surrounding medium to monitor changes in the optical properties of the environment. Since the refractive index of a given solution can be strongly influenced by temperature, refractive index sensing must be combined with simultaneous temperature monitoring to produce useful findings. To address this requirement, a variety of optical fiber-based sensing approaches have been developed [50].

2.5 Ferroelectric Materials

The phenomenon of ferroelectricity was discovered in 1921 by J. Valasek who was investigating the dielectric properties of Rochelle salt. Ferroelectrics are essential components in a wide spectrum of applications, ferroelectrics and, more widely, polar materials have now been used for several years in RF devices and in nonvolatile memories[61]. Ferroelectric materials are currently being developed for various purposes, especially as part of microelectronic devices Ferroelectric materials consist of complex chemical compounds and up to this day there are nearly 100 inorganic compounds [62].Ferroelectrics are typically materials with high dielectric constant values, leading to applications as capacitors. They carry a spontaneous electric polarization that can be switched between two or more states using an electric field [63].

2.5.1 Applications for Ferroelectric Materials

- Capacitors
- Non-volatile memory
- Piezoelectrics for ultrasound imaging and actuators
- Electro-optic materials for data storage applications
- Thermistors
- Switches known as transchargers or transpolarizers
- Oscillators and filters
- Light deflectors, modulators and displays

Ferroelectric materials possess spontaneous polarizations that are usually originated from the collective displacement of ions in the crystals. Applying an electric field leads to polarization reversal that is coupled with a strain response known as the piezoelectric effect. Because of their multi functionality, ferroelectric materials are widely used in nonvolatile memory, ultrasonic imaging systems and many other devices. Ferro electricity was originally discovered in Rochelle salts4 and later in several other molecular systems.

However, the rapid development of the field took place only after the discovery of Ferro electricity in perovskite oxides [64]. Electrical current I in materials is expressed by Ohm's law as I =V/R, where V and R, are potential difference and resistance respectively. When the equation is normalized by the sizes of materials, Ohm's law can be expressed as J= $\mathcal{E}E$,where J, Ɛ, E are current density, permittivity, and electric field strength. The permittivity Ɛ is generally dependent on materials themselves and a useful parameter, which varies by a factor of over 10^{20}, to categorize materials into metals, semiconductors and insulators [65].

The most widely used inorganic ferroelectric materials such as perovskite barium titanate and lead zirconate titanate, while showing excellent performance characteristics, are intrinsically limited in their applicability due to the presence of heavy metals. As ferro electricity is defined by the switchable polarization under the influence of an external electric field [66]. Ferroelectric materials have long captured scientific concerns because of their important applications as a basic element of sensing devices and memories. With the increasing demand on flexible devices and printed electronics, ferroelectrics should be flexible, thin, lightweight, and environment-friendly, which contain heavy metals, have almost no mechanical flexibility and require energy-intensive fabrication processes. Observing numerous ferroelectric vortex modes in inorganic perovskites, small-molecule organic ferroelectrics have made great progress including large spontaneous polarization, high Curie temperature, and ultrafast polarization switching [67]. Ferroelectric materials are characterized by a permanent electric dipole that can be reversed through the application of an external voltage, but a strong intrinsic coupling between polarization and deformation also causes all ferroelectrics to be piezoelectric, leading to applications in sensors and high-displacement actuators. A less explored property is flexoelectricity, the coupling between polarization and a strain gradient. Pure mechanical force can, therefore, be used as a dynamic tool for polarization control and may enable applications in which memory bits are written mechanically and read electrically [13]. Ferroelectric materials that exhibit a stronger Pockels effect. Barium titanate ($BaTiO_3$,BTO)is among the most promising ferroelectric materials for EO applications, because of its strong Pockels effect The slots can be filled with nonlinear functional materials introducing the Pockels effect [68]. A homogeneous ferroelectric single crystal exhibits only two remnant Interest in ferroelectric properties, materials and devices has been considerable over the last 10 years [14]. As optical materials applications are expanding, the need for novel optically functional and transparent materials increases. These needs range from high performance, all optical switches for future use in optical computing as switching and amplification; the materials must be integrated into existing structures such as waveguides and optical fibers. As such, films and fibers are of great interest as the final form of these novel materials. Nano composite materials show great promise as they can provide the necessary stability and process ability for these important applications. Nonlinear optical materials can be useful for all optical switching and wavelength manipulation. Optical Absorption as a Measure of Particle Size and Distribution. Currently, semiconductor Nano crystals are primarily studied for their enhanced optical properties [69]. Properties of ferroelectric materials, symmetry considerations, coupling of electro-mechanical and thermal properties, and definitions of relevant ferroelectric phenomena are provided. On the other hand, problems associated with applications of ferroelectric materials, such as polarization fatigue, ageing and field and frequency dependence of the piezoelectric, elastic and dielectric properties, generated intensive research of the fundamental properties of ferroelectrics [70]. In various fields of industry and science, piezoelectric and ferroelectric materials are frequently used. The piezoelectric effect is used in the sensors. Aside from piezoelectric applications, ferroelectrics' optical, thermal, and electrical properties are used in a wide range of systems and components [71]. Ferroelectricity is a property of some non-conducting crystals, or dielectrics, that display spontaneous electric polarization that can be reversed in direction by applying a suitable electric field. All ferroelectric crystals are pyroelectric and piezoelectric by definition. Many lose these polar properties at the transition or Curie temperature Tc a nonpolar phase above Tc is the so-called para electric phase Ferro electricity. ferroelectrics, the piezoresponse of organic materials still do not match that of piezo ceramics such as BTO [72]. Transitions accompanied by switchable dielectric behaviors, reversible structural phase transitions can be defined as the local or micro mutual transformations in crystal structures. Because they are often accompanied by many interesting physical response signals during the phase transitions processes, ferroelastic materials, ferroelectric materials, energy storage, temperature controlling, data communication, infrared acquisition, signal processing and nonlinear optical (NLO) materials [73].

2.5.2 Lithium Niobate

Dispersion of short optical pulses propagating in optical fibers is one of the main limiting factors for high bit rate transmission. When the pulses are produced by a chirped source like a directly modulated semiconductor laser, this effect may even be worse. This explains why external modulation is usually preferable than direct modulation in 1.55 m telecommunication systems. $LiNbO_3$ Mach–Zehnder modulators (MZMs) have known an increasing interest, because their negligibly small wavelength dependence makes them suitable for both time division multiplexing and wavelength division multiplexing optical transmission systems[74]. Many electro-optic and frequency converter devices rely on ferroelectric materials like lithium niobate and lithium tantalate. 90° walls can also arise in tetragonal systems, where the latter refers to walls that separate two perpendicular polarization directions, which is analogous to crystallographic twinning. Any electric field created by a displacement of charges controls the refractive index by the linear electro-optic (Pockels) effect, according to several experimental and theoretical investigations on the process of polarization reversal and domain dynamics in ferroelectric crystals. Any inhomogeneous illumination that results in a spatially modulated charge carrier photo excitation will cause a redistribution of charge with accompanying space-charge electric field and refractive index modification due to charge-carrier diffusion (or drift in an applied field). When the word photorefractive effect is applied to this class of materials, this is the origin and meaning of the phrase [75]. An electric field produces electron or crystal-lattice displacements in the EO effect, which results in a change in refractive index. Devices based on this phenomenon are predicted to respond very quickly. $LiNbO_3$ is a unique EO crystal in that it can be grown on large wafer substrates and has a low dielectric constant, quick device responses, and low power consumption. The relationship between the refractive index n and the electric field E is written as:

$$1/n^2 = 1/n_0^2 + rE + hE^2 + \cdots \qquad (2.1)$$

where no represents the refractive index in the absence of an electric field, r represents the electro-optic coefficient, and h represents a higher order electro-optic coefficient. The $LiNbO_3$ crystal is a ferroelectric crystal that displays electric dipoles (spontaneous polarization) even when no electric field is applied. Above a particular temperature, known as the Curie temperature, the electric dipole vanishes. The crystal shows an EO effect where the refractive index changes linearly with the applied field. This type of electro-optic effect is known as Pockels effect. Low loss planar waveguides can be fabricated on $LiNbO_3$ substrates by several methods. The refractive index of the core portion of the waveguide is made higher than that of the surrounding region, which confines light. Optical-axis alignment issues associated with bulk optics are avoided by channeling light into planar waveguides. This sort of device is made utilizing procedures similar to those used to make integrated circuits (ICs). This makes it possible to mass-produce somewhat complicated planar lightwave circuits (PLCs). Almost all guided-wave optical switching technologies have been tested and proven utilizing $LiNbO_3$ during the course of its long existence. Lithium Tantalate (LiTa03 or LT) has a crystal structure and properties similar to lithium nitrate (LN). However, because its Curie temperature is lower than (655 °C), fabricating good optical waveguides is more difficult. As a result, LT crystals are not as often employed in optical switching as LN crystals. This chapter provides a quick overview of some LT devices. Lead Zirconate Titanate (Pb(Zr, Ti)03, or PZT) and Lead Lanthanum Zirconate Titanate [(Pb, La)(Zr, Ti)03, or PLZT] are two more ferroelectric materials utilized in optical switches. Electro-optic coefficients are one order of magnitude higher in these materials than in LN. Low-loss waveguides are difficult to fabricate, which limits their application in optical switching. Waveguide loss could be reduced as a result of recent advancements in fabrication technologies [76].

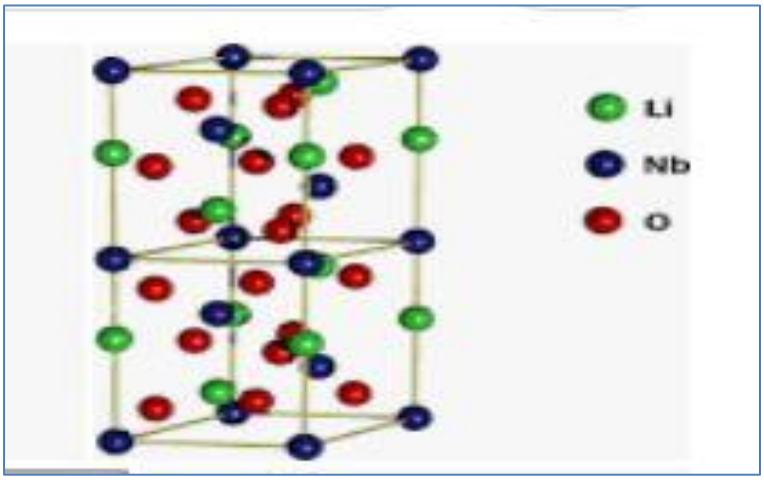

Figure (2.4):Structure of Lithium niobate [77]

2.5.3 Perovskite

Recent developments show the potential applications of organic- in organic perovskite materials in electronics, light sources, photo voltaics, and even ferroelectrics .Because of their distinct structure, hybrid materials combine the benefits of organic molecules and advantageous characteristics of crystalline inorganic solids at a molecular level. We report the discovery of a single-phase organic-inorganic perovskite piezo- electric of trimethy lchloromethyl ammonium trichloromanganese that exhibits a piezoelectric coefficient [72] . Because of their superior ferroelectric and other features, inorganic perovskite ferroelectrics are frequently employed in nonvolatile memory components, capacitors, and sensors. Mechanical flexibility, low weight, ecologically friendly production, and low processing temperatures are all advantages of organic ferroelectrics. Despite the fact that the first ferroelectric, Rochelle salt, was discovered about a century ago, there are few instances of highly desirable organic perovskite ferroelectrics. The term "perovskite" comes from the mineral $CaTiO_3$, which was discovered in 1839 by Gustav Rose. The most abundant minerals in the Earth's interior are magnesium silicate perovskite and calcium silicate perovskite. Perovskites have a characteristic three-dimensional structure (3D). ABX3 crystal structure, in which the A cations are located in the 3D corner-sharing framework of BX6 octahedrons (B represents the other cation and X is an anion). There are hundreds of known perovskites, constituting an essential class of functional materials in optoelectronics and microelectronics. Among their numerous attractive properties, ferroelectricity, which is the ability to switch spontaneous polarization (Ps) under an applied electric field, is of particular interest for theoretical studies and is important for a variety of applications. Inorganic perovskites, such as $BaTiO_3$ and $Pb(Zr,Ti)O_3$, dominate applications such as ferroelectric memories, piezoelectric sensors, actuators, capacitors, and nonlinear optical devices . However, the requirements for practical materials Tobe energy efficient, economically in- expensive, and environmentally friendly (“triple E”) motivate the exploration for nontoxic, low- cost, and simple alternatives to inorganic perovskite [78]. Piezoelectric materials are technologically important, and the most used ones are perovskite ferroelectrics. In the recent years, more and more emerging areas have put forward new requirements for piezoelectric materials, such as lightweight, low acoustic impedance, good flexibility, and biocompatibility. In this context, hybrid organic−inorganic perovskite ferroelectrics have emerged as promising supplements, because they combine attractive features of inorganic and organic materials. Among them, hybrid double-metal perovskites have recently been found to exhibit excellent Ferroelectricity. However, their potential as piezoelectric materials has not been exploited. Here, we describe large piezoelectric response [79].

Perovskites are materials described by the formula ABX3, where X is an anion and A and B are cations of different sizes (A is larger than B). The crystal structure of perovskites is depicted in Fig. (2.5). Their crystallographic stability and probable structure can be deduced by considering a tolerance factor t and an octahedral factor μ [80]. It has been founded a family of metal-free organic perovskite ferroelectrics with the characteristic three-dimensional structure [78].

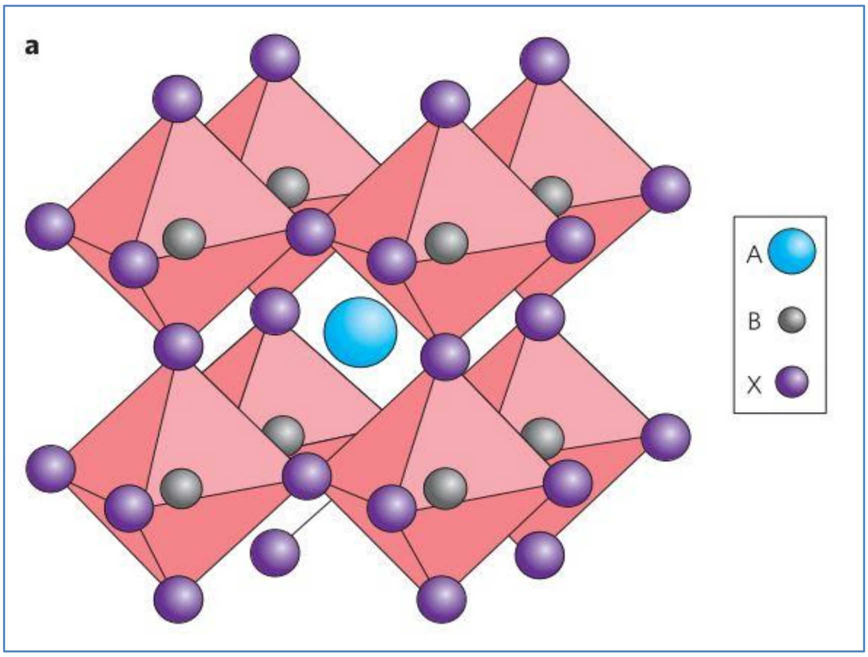

Figure (2.5):perovskite crystal structure[78].

2.5.4 Potassium Nitrate

Potassium nitrate is a chemical compound with the chemical formula KNO_3. It is an ionic salt of potassium ions K+ and nitrate ions NO_3–, and is therefore an alkali metal nitrate. It occurs in nature as a mineral, niter (or nitrate in UK), it is a source of nitrogen, and nitrogen was named after niter. Potassium nitrate is one of several nitrogen-containing compounds collectively referred to as salt peter (or saltpeter in North America) Crystals of Rochelle salt are very peculiar to study due to their ferroelectric nature. The conductivity properties of Rochelle salt are anomalous and the dielectric studies exhibits several dispersions [81].

The structure of Single- crystal determinations of phase III were obtained at 295 and 123 K. Unit cell regained its room-temperature dimensions after warming from 123 K. Phase-III KNO_3 structure can be viewed as the stacking parallel to the c axis of alternating K atoms and planar NO_3 groups. NO_3 groups join the planes of K atoms, where each O is fourfold coordinated to one N and three K. Each K atom has nine O nearest neighbors, with three bonds at 2.813 and six at 2.9092 A˚. Interatomic K—N—K distance alternates from 5.051 to 3.941 along the c axis. The N—O distances increase from 1.245 A˚at 295 K to 1.2533 A˚ at 123 K. The nitrate group has a slight non-planarity, with the N atoms 0.011 A above the O plane and directed toward the more distant K of the K—N—K chain. Nitrates such as KNO_3 important to know the form of KNO_3 or other nitrates in the atmosphere as different phases can display different physical and chemical properties. KNO_3 is also an important ingredient in explosives and propellants and shows promise as a material for random access memory (RAM) devices. [82]. Meanwhile, KNO_3 is widely used as one of the resources for potash fertilizer in agriculture. Therefore, under the consideration of production cost and environmental benignity [83]. There were no visible or biochemical signs of ill health (inappetence, lethargy, shaking or instability) in any sheep fed lathyrus. Several sheep fed the 70% lupin diet had mild diarrhoea, and two were eventually removed from the experiment due to anorexia. Meat from sheep fed lupin tended to be yellower than that from those fed lathyrus ($P = 0.05$). Apart from this, there were no differences in meat quality due to grain type [84].

The explicit dependences of ferroelectric properties upon film thickness or particle size have been known both theoretically and experimentally for many years. As films become thinner, depolarization field effects become important, lowering both Curie temperature T c and spontaneous polarization. For sufficiently thin films (or small particles) both reach zero, and Ferro electricity becomes impossible. It is also possible for Ps to increase near the surfaces of films, resulting in "super polarized" surface layers. This has been treated theoretically using both pseudo-spin models [85]. It is known that KNO_3 has an orthorhombic structure at room temperature and atmospheric pressure, Pnma (Pmcn) – phase II, and crystallizes in the structural type of aragonite with the following lattice parameters: a = 5.4119 Å, b = 9.1567 Å,

c = 6.4213 Å, that is clear in figure (2.6)[86].

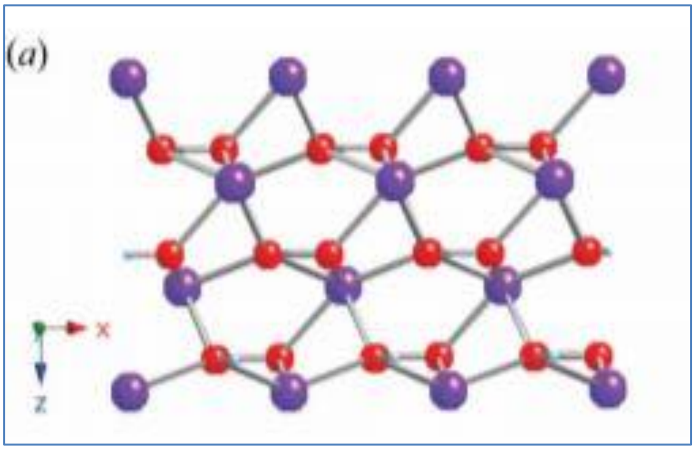

Figure (2.6):Structure of Potassium nitrate[87].

Chapter Three

Numerical analysis

of MZM

3.1 Introduction

The classical macroscopic electromagnetic field is described by four vector functions of position x and time t denoted by Ē, D, H and B. The electric and magnetic field strengths are defined by the basic field vectors Ē and H, respectively. The electric displacement and magnetic induction are the vector functions D and B, which will eventually be excluded from the description of the electromagnetic field via suitable constitutive relations. A distribution of sources, consisting of static electric charges and the directed movement of electric charge, known as current, creates an electromagnetic field. A scalar charge density function describes the distribution of charges, while the vector current density function J describes currents. The following equations, which are applied throughout the region of space inhabited by the electromagnetic field, link the field variables and sources, according to Maxwell's equations.[88].

3.2 Maxwell's Equations

These equations represent the state of electromagnetic theory in the mid-nineteenth century, When Maxwell began his work in the mid-nineteenth century, these equations represented the state of electromagnetic theory at the time. They weren't written in such a concise format back then, but their physical content was familiar. Now, it just so happens that these formulations have a catastrophic flaw. It has something to do with the ancient requirement that curl divergence must always be zero. Everything works out when you apply the divergence on the equation (3.3) [89].

$$\nabla \cdot \mathbf{E} = \frac{1}{\epsilon_0}\rho \qquad \text{(Gauss's law)} \qquad (3.1)$$

$$\nabla \cdot \mathbf{B} = 0 \qquad \text{(Gauss's law for magnetism)} \qquad (3.2)$$

$$\nabla \times \mathbf{E} = -\frac{\partial \mathbf{B}}{\partial t} \qquad \text{(Faraday's law)} \qquad (3.3)$$

$$\nabla \times \mathbf{B} = \mu_0 \mathbf{J} + \mathbf{D} \text{ (Ampère's law)} \qquad (3.4)$$

Where $\varepsilon_{\circ}$ Electric field permittivity , D electric displacement , E electric field intensity ,magnetic induction B, J electric current density, μo the permittivity of light in vacuum, ρ the charge density, the electric field E (in volts per meter), the magnetic field H (amperes per meter), D (coulombs for square meters), and the magnetic field density B (amperes per square meter) are related to each other through the equations [90].

So far, the following laws specify the divergence and curl of electric and magnetic fields [91].

$$\nabla \cdot (\nabla \times \mathbf{E}) = \nabla \cdot \left(-\frac{\partial \mathbf{B}}{\partial t}\right) = -\frac{\partial}{\partial t}(\nabla \cdot \mathbf{B}) \qquad (3.5)$$

form Suppose there are no currents ,charges nor magnetization ,then multiplying Faraday's law with μ-1 ,taking the curl and using the constitutive relations and Amperes 'law leads to the nonlinear electromagnetic wave equation of the

$$\nabla \times (\mu(x)^{-1} \nabla \times \mathcal{E}) + \varepsilon(x)\theta_1^2 \varepsilon + \partial_1^2 \mathcal{P}_{NL}(x, \mathcal{E}) = 0 \qquad (3.6)$$

For the electric field Ɛ ,solving this one obtains $\mathcal{D} = \varepsilon\mathcal{E} + \mathcal{P}_{Nt}(x, \mathcal{E})$ by the constitutive relation and Ɓ by time integrating Faraday's law .finally is also determined by the constitutive relation . Equation (3.6) represent to nonlinear forma the left side is zero because the divergence of curl is zero; the right side is zero by virtue of equation (3.2). However when doing the same thing to equation (3.4), getting into trouble:

$$\nabla \cdot (\nabla \times \mathbf{B}) = \mu_0(\nabla \cdot \mathbf{J}) \tag{3.7}$$

The left side must be zero, but the right side, in general, is not. For steady currents, the divergence of J is zero, but when it goes beyond magneto statics Ampère’s law cannot be right. There is another way to see that Ampère’s law is bound to fail for no steady currents. Suppose the process of charging up a capacitor in integral form, Ampère’s law reads.

The problem is on the right side of Eq. (3.6), which should be zero, but isn’t. Applying the continuity equation and Gauss’s law, the offending term can be rewritten [92]

$$\nabla \cdot \mathbf{J} = -\frac{\partial \rho}{\partial t} = -\frac{\partial}{\partial t}(\epsilon_0 \nabla \cdot \mathbf{E}) = -\nabla \cdot \left(\epsilon_0 \frac{\partial \mathbf{E}}{\partial t}\right) \tag{3.8}$$

The combination of ($\partial E/\partial t$) with J, in Ampère’s law. would be just right to kill off the extra divergence:

$$\nabla \times \mathbf{B} = \mu_0 \mathbf{J} + \mu_0 \epsilon_0 \frac{\partial \mathbf{E}}{\partial t} \tag{3.9}$$

Apart from curing the defect in Ampère’s law, Maxwell’s term has a certain aesthetic appeal: Just as a changing magnetic field induces an electric field Faraday’s law, so a changing electric field induces a magnetic field. Of course, theoretical convenience and aesthetic consistency are only suggestive there might, after all, be other ways to doctor up Ampère’s law. The real confirmation of Maxwell’s theory came in 1888 with Hertz's experiments on electro- magnetic waves. Maxwell called his extra term the displacement current (D)

$$\mathbf{J}_d \equiv \epsilon_0 \frac{\partial \mathbf{E}}{\partial t} \tag{3.10}$$

(It's a misleading name; ϵo(∂E/∂t) has nothing to do with current, except that it adds to J in Ampère's law) Let us see now how displacement current resolves the paradox of the charging capacitor. If the capacitor plates are very close together, then the electric field between them is:

$$E = \frac{1}{\epsilon_0}\sigma = \frac{1}{\epsilon_0}\frac{Q}{A} \tag{3.11}$$

where Q is the charge on the plate and A is its area. Thus, between the plates:

$$\frac{\partial E}{\partial t} = \frac{1}{\epsilon_0 A}\frac{dQ}{dt} = \frac{1}{\epsilon_0 A} I \tag{3.12}$$

when E is constant, it still have $\nabla \times B = \mu_o J$. In fact, Maxwell's term is hard to detect in ordinary electromagnetic experiments, where it must compete for attention with J—that's why Faraday and the others never discovered it in the laboratory [93]. In an electro optic crystal TE and TM modes can be coupled by application of a modulation voltage. There are two types of modulators using anisotropic crystals. In the first type a voltage that is constant along the direction of wave propagation couples a guided mode to a radiation mode of the orthogonal polarization so that the radiation loss of the guided mode can be controlled by the applied voltage. The modulator of the second type uses voltage-controlled coupling between guided TE and TM modes [94]. Aspects related to vector analysis and electromagnetic fields in free space are examined, taking into account scalar and vector fields, coordinate systems, differential elements of space, vector integration, electric charges, electric and magnetic fields, and Maxwell's integral relations for free space. Vector differential relations and Maxwell's differential relations in free space are considered along with Maxwell's equations and boundary conditions for material regions at rest, static and quasi-static electric fields, static and quasi-static magnetic fields, the Pointing vector, a mode theory of waveguides, TEM waves on two-conductor transmission lines, the analysis of reflective transmission lines, and radiation from antennas in free space [95].

3.3 Modeling and Optimization

In finite element method at COMSOL multiphysics, the mesh design resolved the varying of the electric field and magnetic field, the electromagnetic waves beam envelopes interface can be combined with the electrostatics interface to perform simulations of the properties of an optical waveguide modulator. The design of MZM is implemented in a 2D geometry, the electromagnetic waves beam envelopes interface is formulated assuming that the electric field is defined as the product of a slowly varying envelope function and a rapidly varying phase function [96]

$$\mathbf{E} = \mathbf{E}_1 \exp(-j\mathbf{k} \cdot \mathbf{r}) \tag{3.13}$$

where E1 represents the envelope function, k represents the wave vector, and r represents the position. The envelope function E1 exhibits a spatial fluctuation on a length scale significantly bigger than the wavelength if k is suitably selected for the situation. The wave is well approximated in the straight domains using the wave vector for the incident mode β, which is a good assumption for this model. The wave vector in the waveguide bends, on the other hand, can be expressed as:

$$\beta_2 = \beta(\cos\alpha\mathbf{x} + \sin\alpha\mathbf{y}) \tag{3.14}$$

where β = K_o neff is the propagation constant for the mode, k_o is the vacuum wave number, neff is the effective index of the waveguide mode, α is the angle from the x-axis, and x and y are the unit vectors in the x and y directions, respectively.The wave vector difference is thus [97]

$$\beta_2 - \beta = \beta((\cos\alpha - 1)\mathbf{x} + \sin\alpha\mathbf{y}) \tag{3.15}$$

It is the wave vector difference that determines the phase variation for the envelope field. Thus, the mesh resolves the phase variation well. As an example,

$$(\beta_2 - \beta) \cdot \Delta\mathbf{r} \le 2\pi/N \tag{3.16}$$

where N is a suitably large number, for instance 6. From the relations above, you get that the maximum mesh element sizes in the x and y directions should be:

$$h_{x,max} = \frac{\lambda}{Nn_{\mathrm{eff}}(1-\cos\alpha)} \tag{3.17}$$

and

$$h_{y,max} = \frac{\lambda}{Nn_{\mathrm{eff}}\sin\alpha} \tag{3.18}$$

3.4 Finite Element Method

Finite element method (FEM) is a mathematical method to solve Maxwell equation for electric and magnetic field . Since its application in electrical engineering in 1965 , the FEM has been proven to be a powerful tool for the computation of electromagnetic fields [98]. Quite used to differential equations to describe the phenomena mathematically based on basic physical principles, namely conservation laws in many mechanical engineering problems. Instead of this differential formulation, physical phenomena can be described in terms of minimization of total energy, Finite element formulation can be derived by this vibrational formulation as long as there exists a vibrational principle corresponding to the problem of interest [99]. The finite element model consists of a set of algebraic equations among the unknown parameters (degrees of freedom) of the element [100] .FEM uses Maxwell's partial differential equations (PDEs) at FEM have been used to solve physical problems , fundamental principle of this process depends mainly on four steps . First step that is discretizing a physical object or a solution domain into thousands of small shapes called mesh elements. The finite elements can be defined as one, two, or three dimensional, depending on the study domain of the physical object. Furthermore, the mesh can be generated uniformly or non-uniformly. When there are important regions in the solution domain where the required parameter from studying this physical problem changes rapidly, it is preferable to define a non-uniform mesh; that is, many of the small elements are concentrated in these regions more than in other regions of the solution domain. The second step is finding the governing PDEs in each element of the mesh , that is many of the small elements are concentrated in these regions more than in other regions of the solution domain. Second step is finding the governing PDEs in each element of the mesh. Third step is assembling of all finite elements in the solution domain. Finally, the general solution of the physical problem results from solving all the equations under certain boundary conditions. This computational method is used in many types of waveguide design software to determine EM field profiles and to calculate the guided modes of the waveguide models by using Maxwell's equations. Software of COMSOL Multiphysics is used to design a waveguide model and find its guided modes by using the Mode-Eigenvalue calculate based on the FEM numerical method [101]. Power transformers represent one of the most expensive components in an electricity system. An extensive transmission system with efficient transformers is indispensable to ensure a reliable supply of power. The insulation system age at a normal rate and provide the standard transformer life when a transformer operates at a temperature [102].

3.5 Total Internal Reflection

For incidence angles (measured from the normal to the interface) greater than the "critical angle," a light beam propagating through a transparent medium with a high index of refraction (e.g. a solid glass prism) encounters an interface with a medium with a lower index of refraction (e.g. an aqueous solution) undergoes total internal reflection. The critical angle θc, is given by:

$$\theta_c = \sin^{-1}(n_2/n_1) \tag{3.19}$$

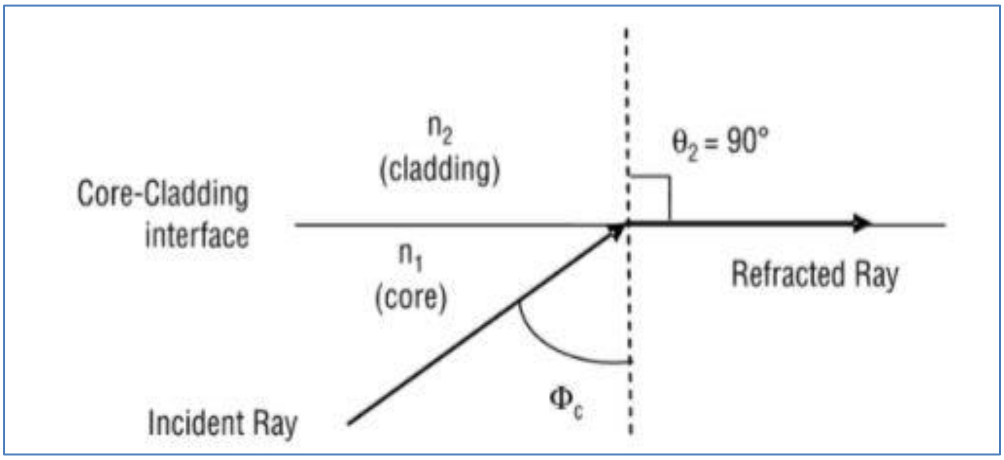

Figure (3.1):Critical angle of two mediums.

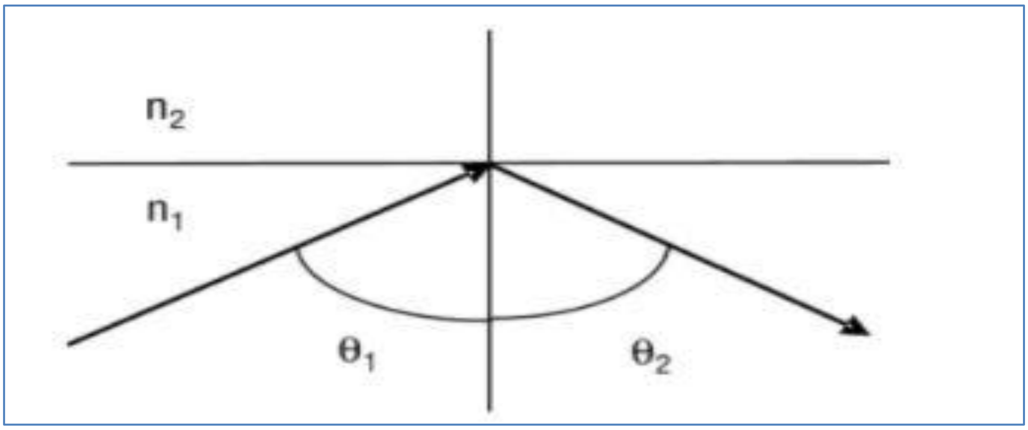

Figure(3.2):Total internal reflection.

The refractive indices of the liquid and solid, respectively, are n2 and n1. Despite the fact that the incident light beam internally reflects heavily at the interface, an electromagnetic field known as a "evanescent wave" penetrates a limited distance into the liquid medium and propagates parallel to the surface in the plane of incidence. Fluorescent molecules that may be present near the interface can be excited by the evanescent wave. This phenomenon has been regarded as experimental proof of the evanescent wave's existence. With perpendicular distance z from the interface, the evanescent electric field intensity I(z) decays exponentially [103] :

$$I(z) = I_0 e^{-z/d} \tag{3.20}$$

Where:

$$d = \frac{\lambda_0}{4\pi}[n_1^2 \sin^2\theta - n_2^2]^{-1/2} \tag{3.21}$$

For angles of incidence $\theta > \theta c$ and light wavelength in vacuum. Depth d is independent of the polarization of the incident light and decreases with increasing θ. Except for $\theta \rightarrow \theta c$ (where $d \rightarrow \sim\infty$), d is on the order of λ_0 or smaller [103]. The incident light polarization, which can be either ‘s' (polarized normal to the plane of incidence formed by the incident and reflected rays) or ‘p' (polarized parallel to the plane of incidence formed by the incident and reflected rays), determines the polarization (i.e. the vector direction of the electric field) of the evanescent wave (polarized in the plane of incidence). The evanescent electric field vector direction remains entirely normal to the plane of incidence for s-polarized incident light. The evanescent electric field vector direction remains in the plane of incidence for p-polarized incident light, but it ‘cartwheels' along the surface with a nonzero longitudinal component (see Figure (3.3)) The absence of a longitudinal component distinguishes evanescent light from freely propagating subcritical refracted light. As the incidence angle is decreased from the supercritical to the critical range, the longitudinal component approaches zero [104].

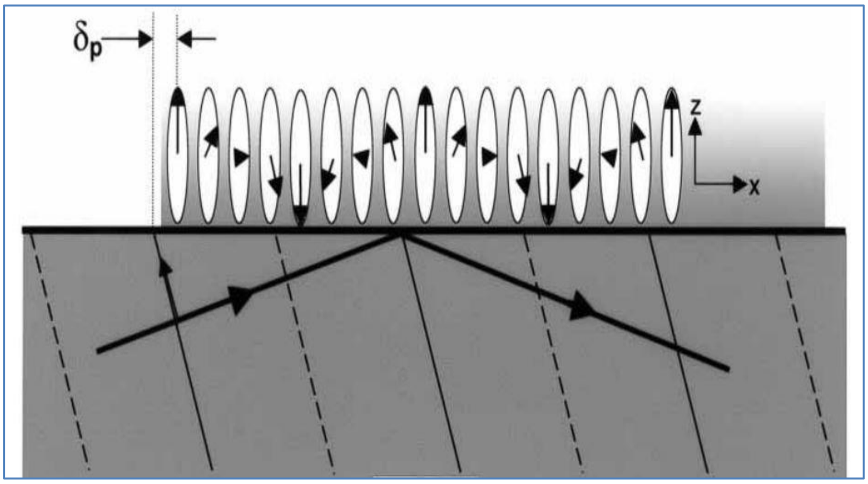

Figure (3.3): Schematic drawing of the evanescent polarization resulting from incident light [104].

The optical effect of the total internal reflection fluorescence (TIRF) is well adapted to the investigation of molecular and cellular events at liquid/solid interfaces. Total internal reflection spectroscopy for optical absorption investigations (also known as attenuated total reflection or ATR) was invented before fluorescence and is commonly utilized in surface chemistry research. Raman spectroscopy, X-ray fluorescence, infrared absorption spectroscopy, and light scattering have all been integrated with total internal reflection optics. Hirschfield presented the total internal reflection fluorescence for solid/liquid surfaces, Tweet et al for liquid/air interfaces, and Carniglia & Mandel for high refractive index liquid/solid interfaces as a technology for selective surface illumination. TIRF has been used in conjunction with a number of other traditional fluorescence techniques [105]. Many applications, such as absorption spectroscopy, thermal imaging, and free-space communication, are possible in the mid-infrared (MIR) region, which is commonly characterized as wavelengths ranging from 2 to 20 m. In this range of wavelengths, because of the occurrence of atmospheric transmission windows in these bands, the wavelength areas = 3–5 m and = 8–12 m are particularly important. Other approaches that rely on sensing changes in refractive index but lack specificity to identify the individual analyte have a significant advantage over absorption-spectroscopy-based detection. The analyte composition can be assessed subjectively and quantitatively using absorption spectroscopy, which detects the optical attenuation when light passes through the analytes at their respective absorbance wavelengths. Although overtones of molecular vibration signatures can be detected by well-developed absorption spectroscopy techniques in the near-infrared (NIR) and visible wavelength domains (2 m), fundamental chemical absorption cross sections are orders of magnitude larger in the MIR than in the NIR and visible, so moving from NIR to MIR can increase detection sensitivity [106].

Chapter Four

Results and Discussions

4.1 Introduction

In this chapter, by using COMSOL Multi- physics analysis software, a study and simulation of many parameters that could influence .MZM operation based three ferroelectric materials were realized as following: There are three materials in this study :

1) Lithium niobate($LiNbO_3$).
2) Perovskite (strontium titanite) ($SrTiO_3$).
3) Potassium nitrate (KNO_3).

Some optical properties are listed in Table (4.1) where n-core and n-clad are core and clad refractive indices, respectively.

Table (4.1): Refractive indices of ferroelectric materials.

Material	Chemical form	n-core	n-cladd
Lithium niobate	$LiNbO_3$	2.22	2.2
Perovskite	$SrTiO_3$	2.3	2.28
Potassium nitrate	KNO_3	2.12	2.1

4.2 Results

MZM design is illustrate in figure (4.1):

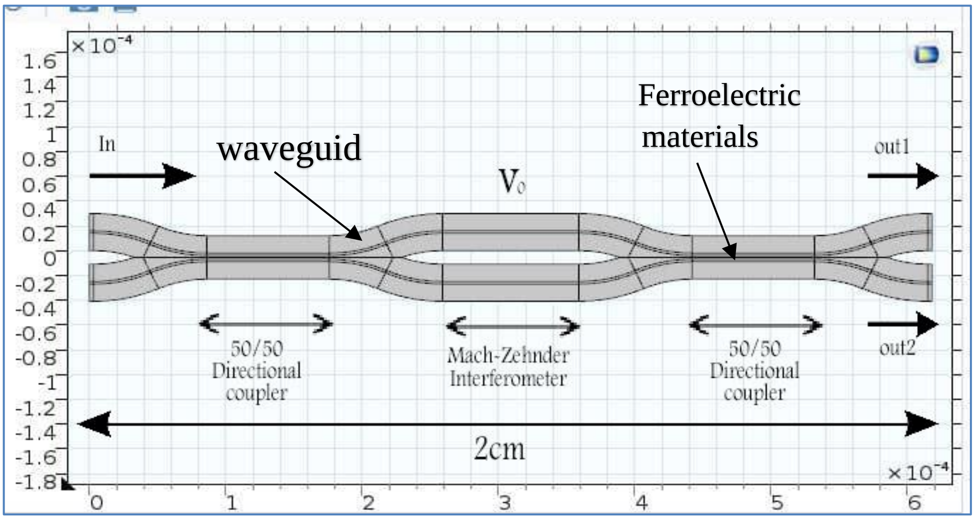

Figure (4.1): Schematic diagram of MZM modulator

Table (4.2): Parameters of the model

Name	Expression	Value	Description
wl	1.55[um]	1.5500E-6m	Wavelength
f0	c_const/wl	1.9341E141/s	Frequency
w	2[um]	2.0000E-6 m	Waveguide width
w-tot	30[um]	3.0000E-5 m	Total waveguide width
d0	2*wl	3.1000E-5 m	Initial straight waveguide
dy_bend	0.6*w_tot	1.8000E-5 m	Total displacement in y-direction at S-bend
r0	2.5[mm]	0.0025 m	Bend radius
alpha	0.084878[rad]	0.084878 rad	Bend angle
dx_bend	4.2366e-4[m]	4.2366E-4m	Total length in the x-direction for S-bend
d-mz	2[cm]	0.02 m	Length of Mach-Zehnder waveguides
hx	wl/(6*n_core)/(1-cos(alpha))	3.1200E-5 m	Maximum element size in x-direction
hy	wl/(6*n_core)/sin(alpha)	1.3249E-6 m	Maximum element size in y-direction
dy-wg	3[um]	3.0000E-6 m	Distance between directional coupler waveguides
r13	30[pm/V]	3.0000E-11C/N	Electro-optic coefficient
v0	100[v]	100 V	Applied voltage
epsr	35	35	Low-frequency relative permittivity

Three parameters were studied for MZM based ferroelectric materials, which are:

4.2.1 Coupling Length

A) $LiNbO_3$

When a potential of (100)volt supplied over one path length(port 1) of MZM based $LiNbO_3$, with(1.5) µm width of the waveguide , the output power difference was zero between the two output arms and this means that the output power is divided equally on the two arms(port2) of MZM as displayed in figures (4.2a and b).

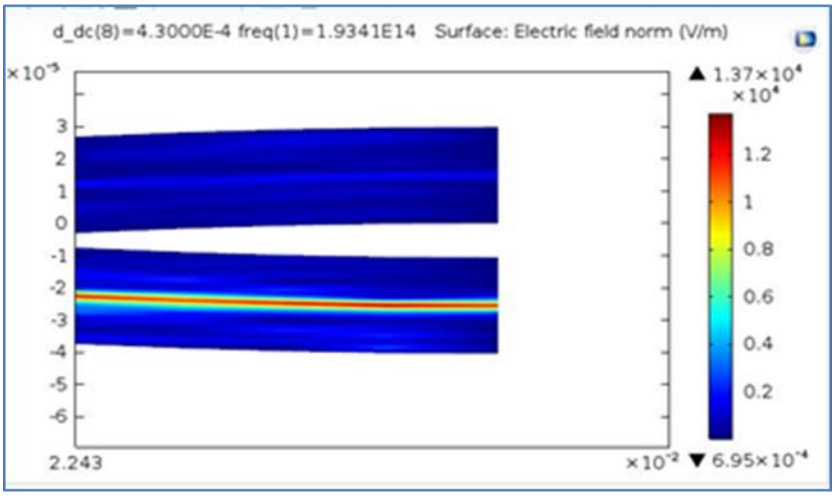

Figure (4.2a):Electric field of the waveguide of two arms of MZM bend radius 2.5mm ($LibNO_3$)the width of the wave 1.5µm.

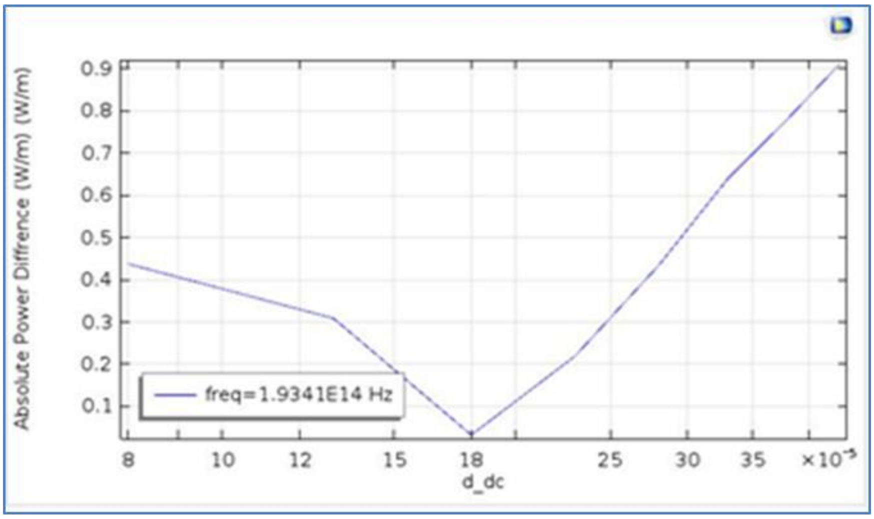

Figure (4.2b):Absolute value of power difference versus length of directional coupler .wave width 1.5µm.

Looking at figure (4.2a)it is clear the electric field of two arms of MZM ,and then figure(4.2b), the relation between the absolute value of power difference in y-axis and the directional coupler (the distances of the coupler d_dc)in x-axis ,we can see the value of d-dc equal (180µm) versus (0.45W/m)of power difference .

When the width of the waveguide change to another value (2 µm),the result is different from the state one as illustrated in figures(4.3a,b),and it is easy to see that .we can observe that the absolute power value is (0.75w/m) and the length of directional coupler is (308 µm) for $LiNbO_3$ that give a zero-power different.

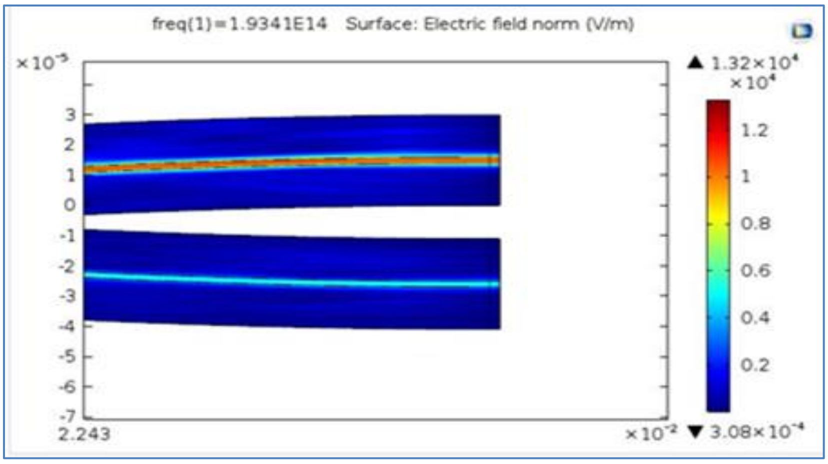

Figure (4.3a): Electric field of MZM based $LiNbO_3$ at bend radius 2.5mm.

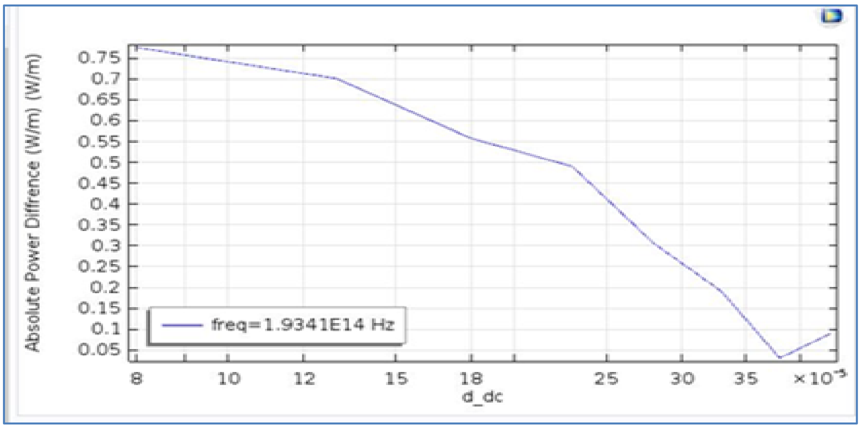

Figure (4.3 b): Absolute value of power difference (y- axis) versus directional coupler length d-dc (x-axis) of MZM based $LiNbO_3$.

Then changing the width of the waveguide to 2.5µm, that mean increase the width of the wave and obtain another result, that is clear in figure (4.4a,b):

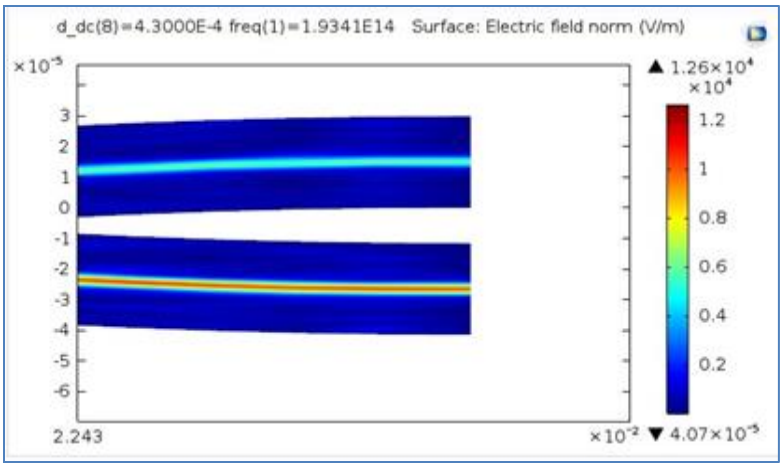

Figure (4.4a):Electric field of the wave guide of two arms of MZM (LibNO$_3$),the width of the wave guide is 2.5μm

From figure (4.4a), the electric field of two arms of MZM we notice the variable shape of the electric field, the analysis of this state beyond to the spectrum of the electric field in the two arms of MZM based of LiNbO$_3$.

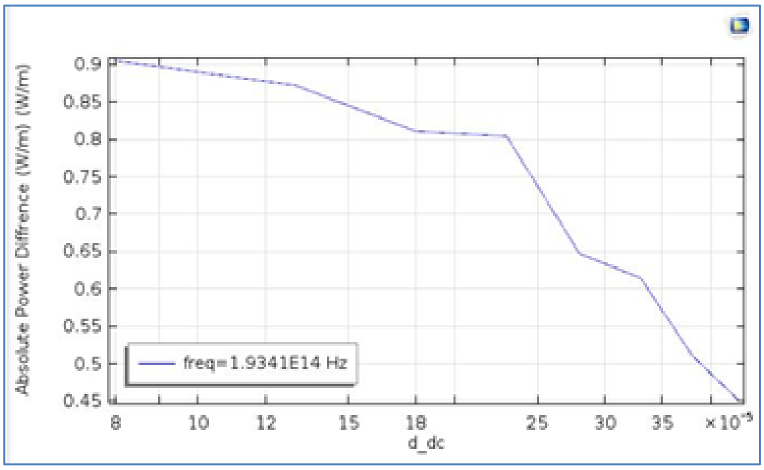

Figure (4.4b): Absolute value of power difference versus directional coupler (waveguide width 2.5μm).

From figure (4.4b) the value of the directional coupler equal(400 μm) versus (0.9 W/m)of power difference .When comparing the three states of changing, we get the optimizing MZM of LiNbO$_3$ which has the shorter directional coupler ,that is clear the MZM when the wave width is (1.5µm)is the optimizing . Any peak of line or the curve in the figures attributed to the material, and the behavior of the substance.

B) $SrTiO_3$

In this section ,the relation between coupling length of MZM and power difference has been studied for $SrTiO_3$,when the waveguide is (1.5µm),bend radius is 2.5mm and applied voltage is (100V),so the results are different and the study is the same, as shown in figures (4.5a,b):

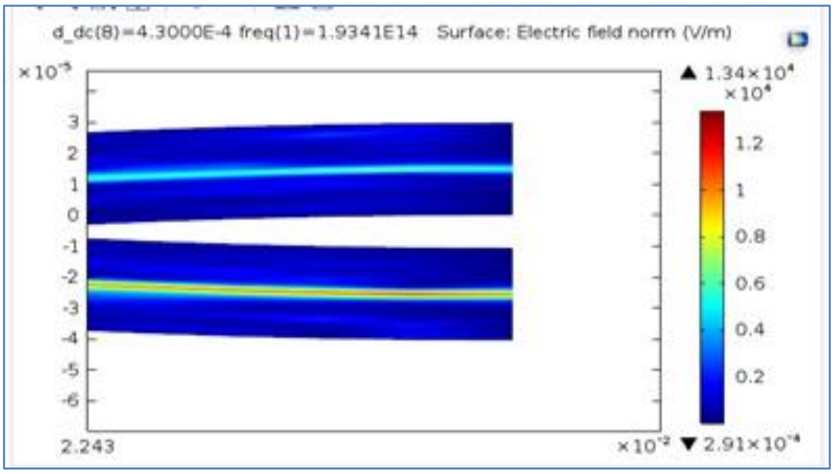

Figure (4.5a):Electric field of MZM $SrTiO_3$,the wave guide width is 1.5µm.

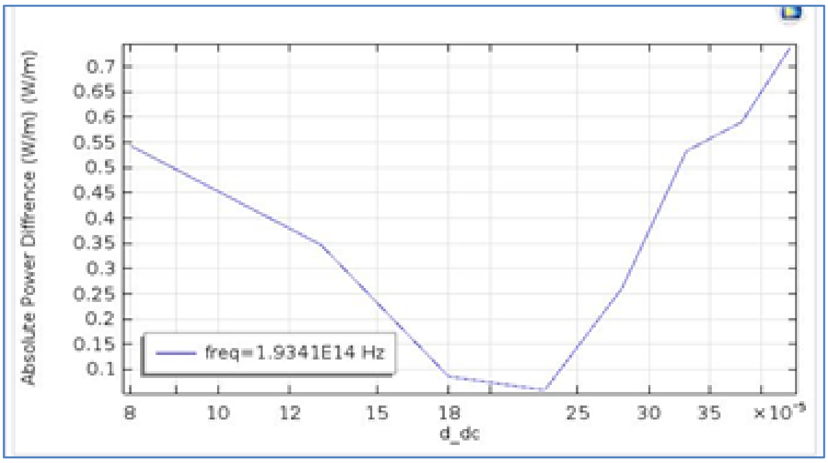

Figure (4.5b): Absolute value of power difference versus directional coupler of MZM, the width of waveguide is 1.5µm

Figure (4.5a) shows that the electric field of the two arms of MZM based $SrTiO_3$ when the width of the wave equal (1.5μm), then figure (4.5b) clearly appear the value of the directional coupler equal (250 μm)versus (0.55W/m) of power difference .When changing the width of the waveguide to (2μm) another result s of the same materials are gotten .Furthermore, figure (4.6a) shows the electric field norm for the wave propagating in the S-shaped bend with bend radius of 2.5mm. The applied voltage was (100) volt for MZM based $SriTO_3$, the wave follows the waveguide in the bend.

The directional coupler structure operates as 50/50 couplers and that indicate a half of the incident power exit from each one of the two output arms. Figure (4.6b) illustrates the relation between the output power difference (the absolute value 0.75w/m) and length of directional coupler. A coupling length of (405 μm) for MZM with $SriTO_3$ crystals gives a zero power difference between the two arms. This result indicates that MZM output power is equally divided on both output ports. When changing the width of the wave to (2μm) obtaining the results in figure (4.6a,b):

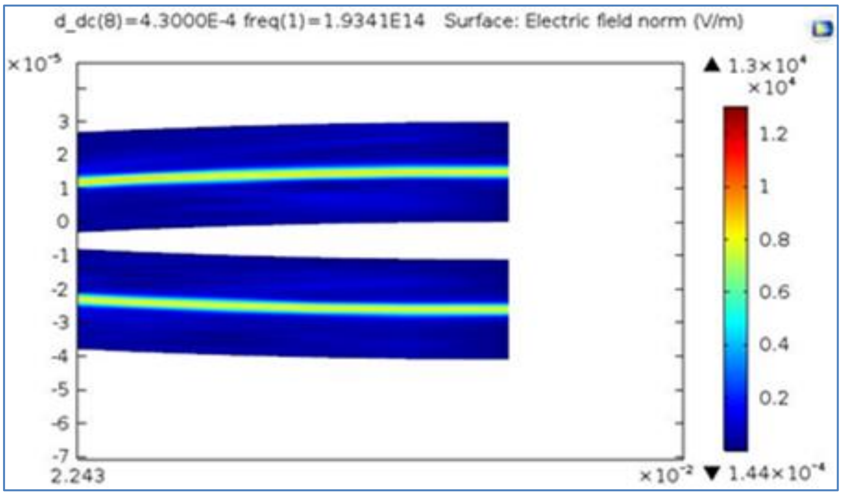

Figure (4.6a):Electric field of MZM $SrTiO_3$,the width of wave is 2μm.

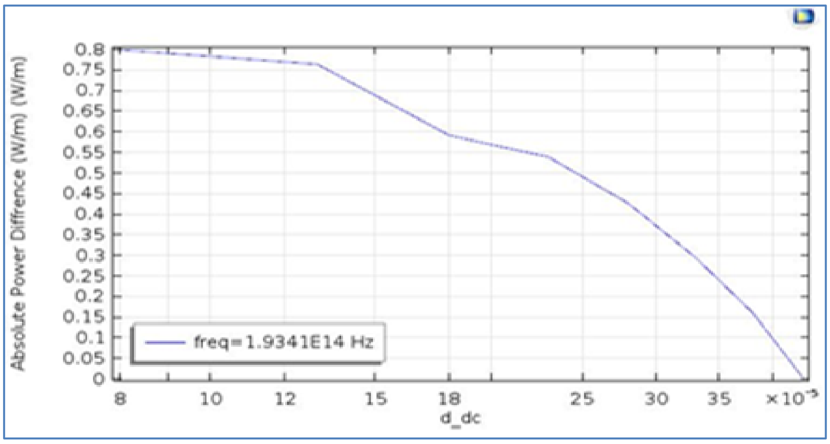

Figure (4.6b): Absolute value of power difference (y- axis) versus directional coupler length d-dc (x-axis) of MZM based $SrTiO_3$.

From the figures of the electric field, which explain the effect of the electric field of optical fiber and the propagating of the wave guide in S-bend where the length of MZM is very important parameter in changing the strength of the evanescent field, in this study the length is 2cm.

Later the width of the wave change to 2.5μm ,the result is changed too, this is represented in figures (4.7a,b)

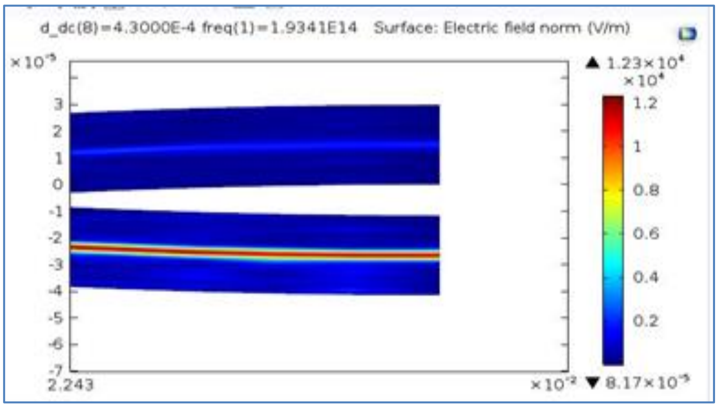

Figure (4.7a):Electric field of MZM $SrTiO_3$,the width of wave is 2.5μm

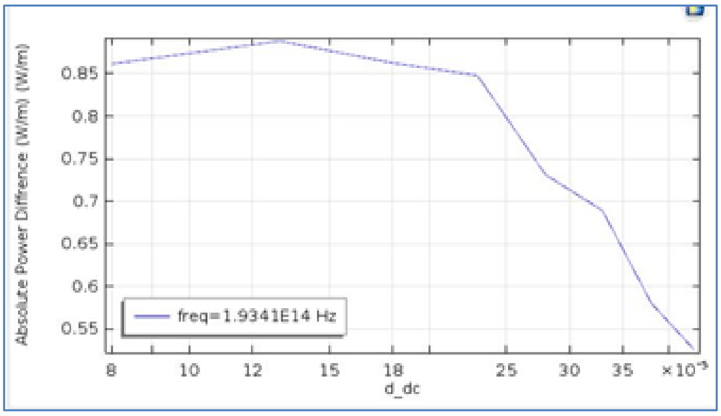

Figure (4.7b): Absolute value of power difference versus directional coupler, the waveguide width is 2.5 µm

The absolute value of power difference is (0.85w/m) and the directional coupler's length is (405µm). At this value the output power difference at the two arms is zero. The optimizing MZM based $SrTiO_3$ was when the width of the waveguide was (1.5µm) because the state has the shorter length of directional coupler.

C) KNO_3

The same parameters gave the results in figures (4.8 a, b),(4.9 a,b),(4.10a,b). As in the previous materials we make the width of the waveguide (1.5µm), the we get the result in figures (4.8a,b):

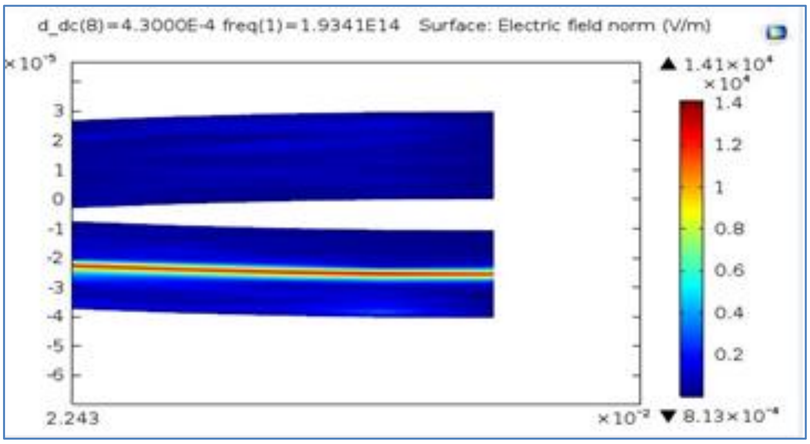

Figure (4.8a):Electric field of the wave of two arms of MZM for KNO_3,the wave width 1.5µm.

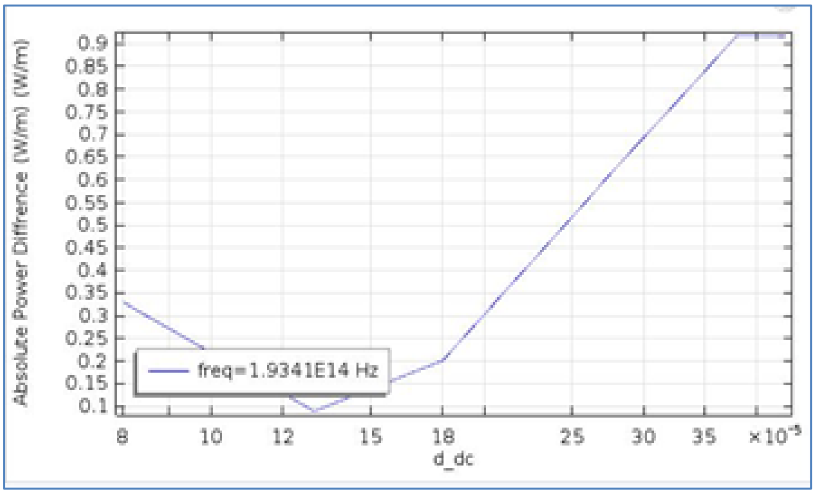

Figure (4.8b): Absolute value of power difference versus directional coupler, the waveguide width 1.5µm

From figure (4.8a), we can see the electric field of MZM based KNO_3,the wave split in the two arms of MZM ,then we can see the figure (4.8b) and obtain the relation between the directional coupler in x-axes(130µm) versus power difference in y- axes (0.35 w/m).Later we change the width of the waveguide to (2µm)and the result changed too as illustrated in figures (4.9a,b):

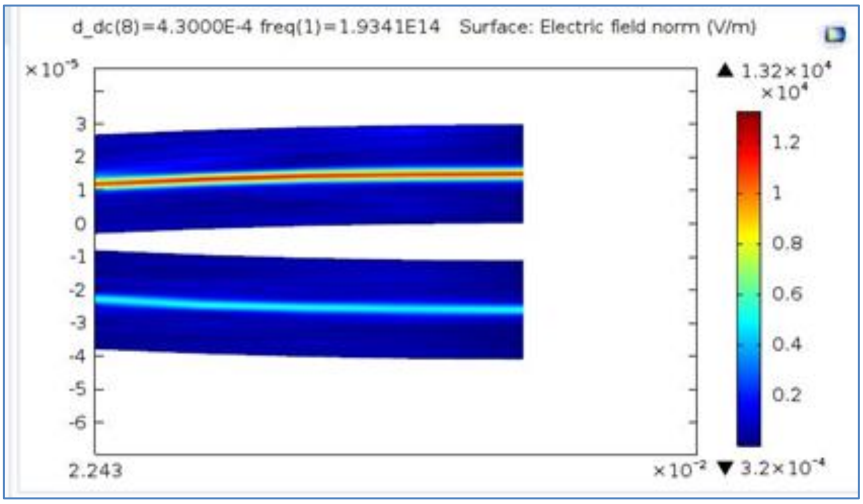

Figure (4.9a): Electric field of MZM based KNO_3.

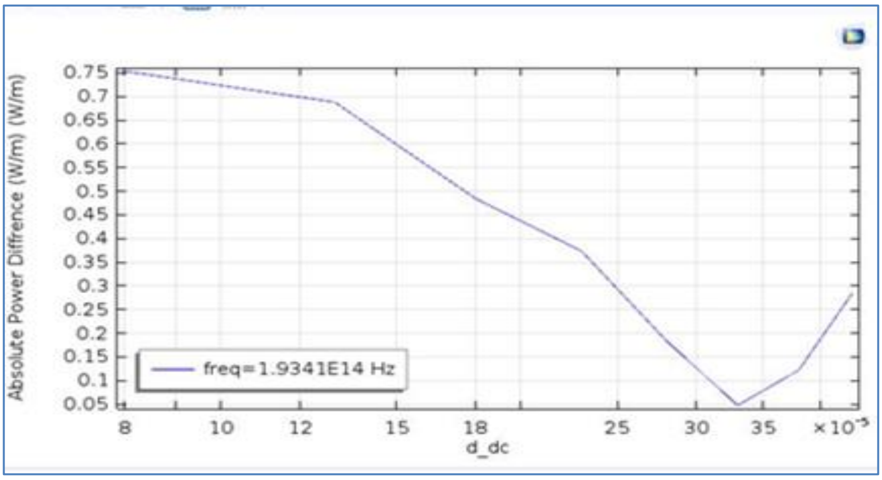

Figure (4.9b):Absolute value of power difference (y- axis) versus directional coupler length d- dc) (x-axis) of MZM based KNO_3.

Looking at figure (4.9a) see the electric field of two arms of MZM, and then see figure (4.9b) directly to find the value of the power difference and coupling length .The values are changing when the width of the wave is changing , (0.75w/m) of power difference gave(304 µm) . Another changing of the width wave ,the width increases to (2.5µm)that effects to the results and gave different value of the power difference and another value of coupling length .these statements are described in figure (4.10a,b):

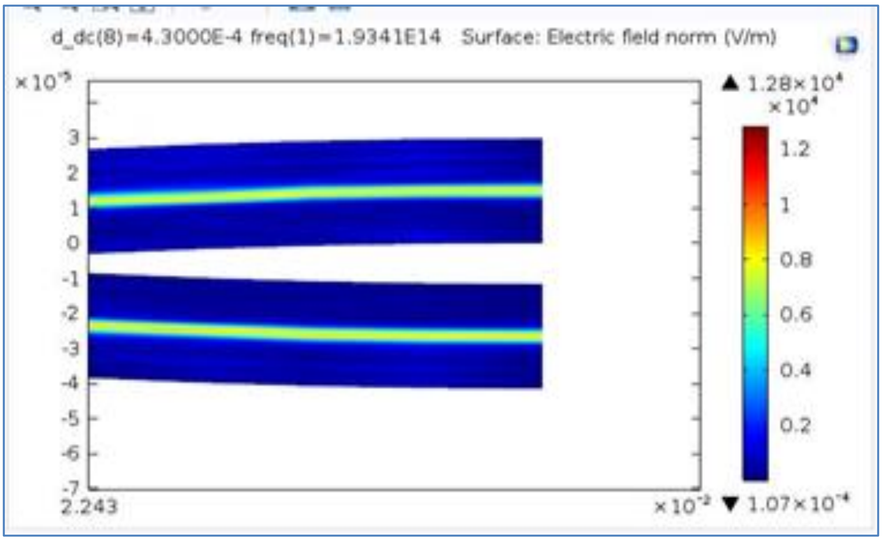

Figure (4.10a):Electric field of the wave of two arms of MZM for KNO_3,the waveguide width 2.5µm.

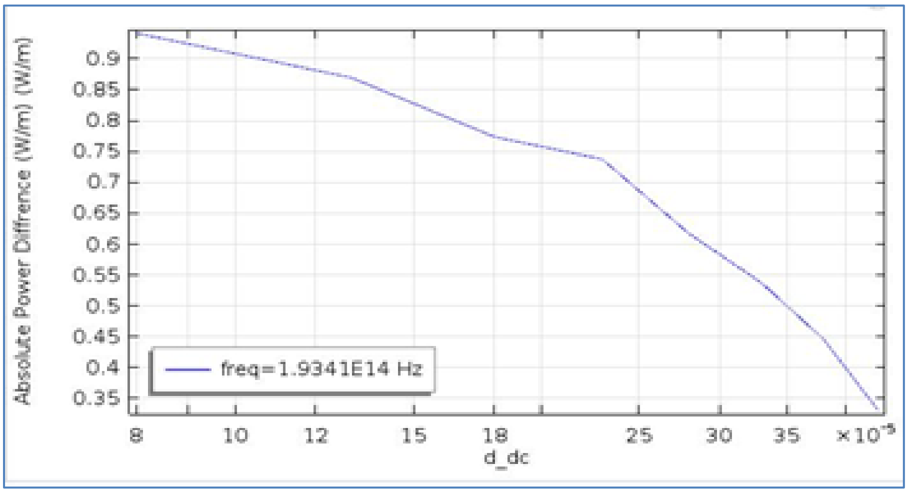

Figure (4.10b): Absolute value of power difference versus directional coupler, the waveguide width 2.5μm.

Clearly from observing the result of figure (4.10b), the value of directional coupler became more than the previous case when the width of the waveguide was 2μm ,the new results show the value of power differences equal (0.95 w/m) versus(450μm)of directional coupler .The best results of KNO_3 were when the width of wave equals (1.5μm) because this width gave shorter directional coupler length (d_ dc).

4.2.2 Total Transmission and Bend Radius

In this part of the work, the relation between transmission and S-shaped bend for MZM. A bend radius curvature for three materials at 2.5mm gives the same results. Where the transmission was approximately 98% of the input power, while the loss is only 2%.The results for each material are shown in figure (4.11a,b),(4.12a,b)(4.13a,b). From figures, the bend radius of curvature (2.5mm) is the smallest value that provides low loss. However, when the bend radius of MZM was less than this value, the output transmission was zero.

A) $LiNbO_3$

For the same parameter for the materials , the relation between the transmission and bend radius has been found .When the waveguide width was (1.5µm)the transmission was 98% and the losses about 2%, that may be an acceptable result .That is clear in figure (4.11a) for the electric field and (4.12b) illustrates the relation between the transmission and bend radius .Firstly the width of the wave was (1.5µm), the results are clear in figures (4.11a,b):

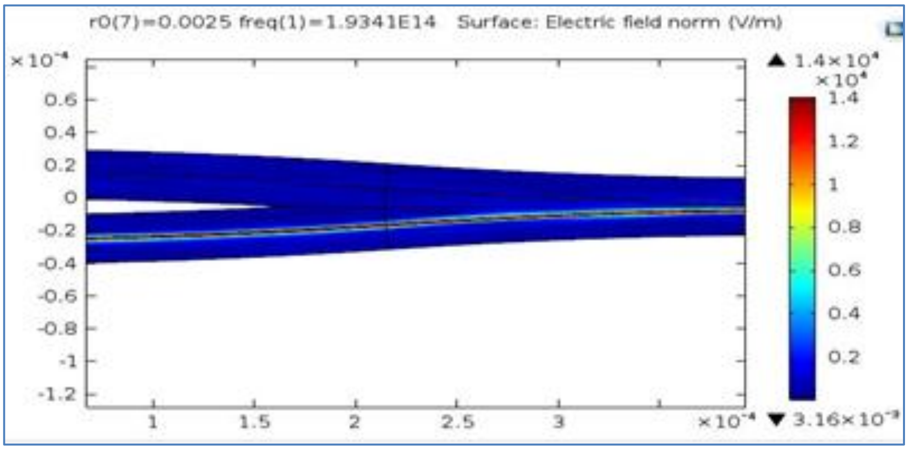

Figure (4.11a):Electric field of the wave guide for two arms of MZM for $LiNbO_3$,the waveguide width 1.5µm.

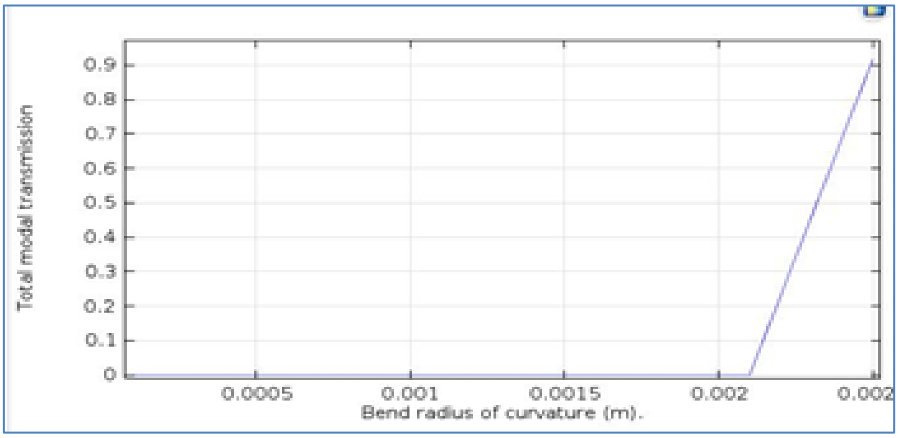

Figure (4.11b): Total transmission versus bend radius of curvature 2.5mm, the waveguide width 1.5µm, $LiNbO_3$.

Then the same relation has been found, but the change in the waveguide width to (2µm), the result is still the same value as seen in figures (4.12a,b)

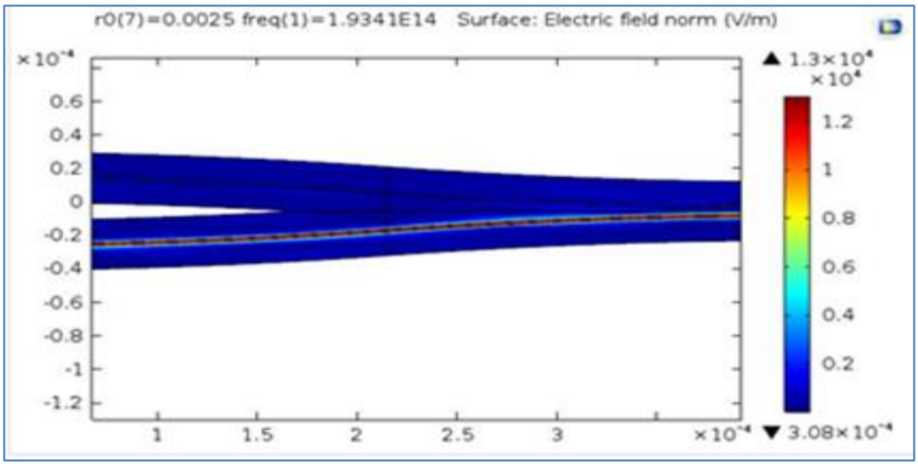

Figure (4.12a):Electric field of MZM based $LiNbO_3$.

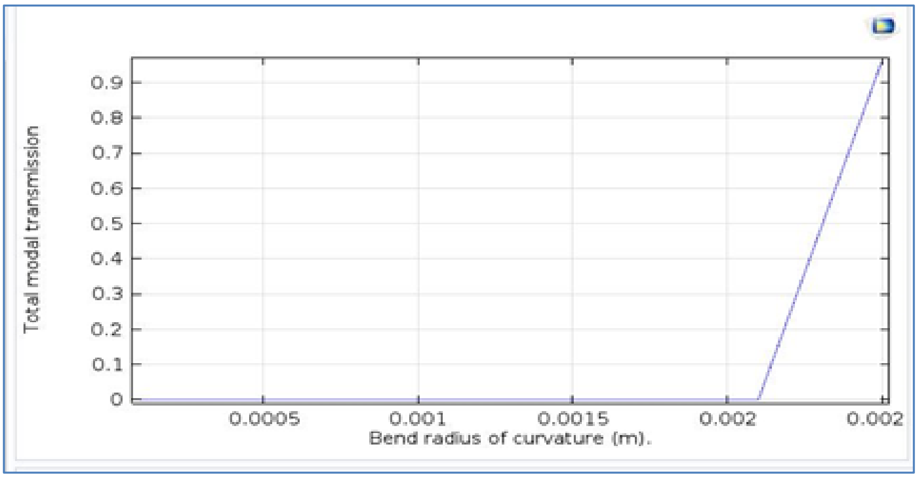

Figure (4.12b): Total modal transmission (y-axis) versus bend radius of curvature (2.5mm) (x-axis) of MZM based $LiNbO_3$.

Then find the same relation, but change the waveguide width to (2.5µm) and the result still the same as seen in figure (4.13a b):

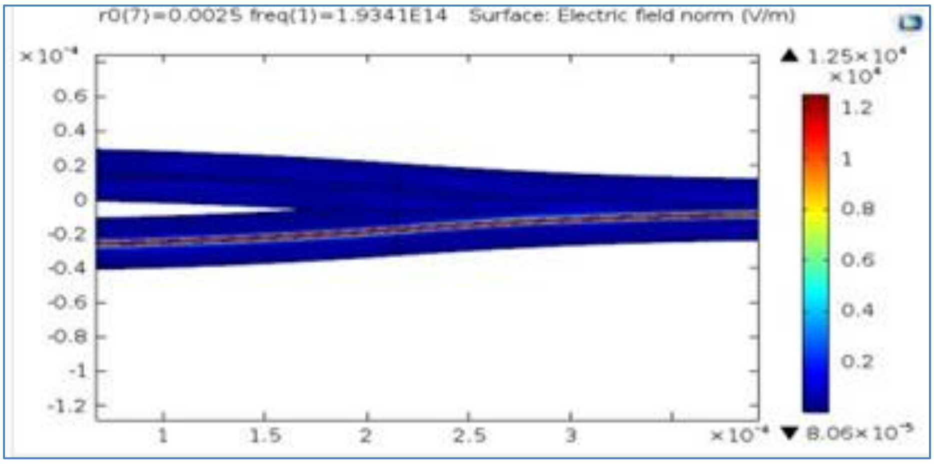

Figure (4.13a):Electric field of the wave guide for two arms of MZM for $LiNbO_3$,the waveguide width 2.5µm.

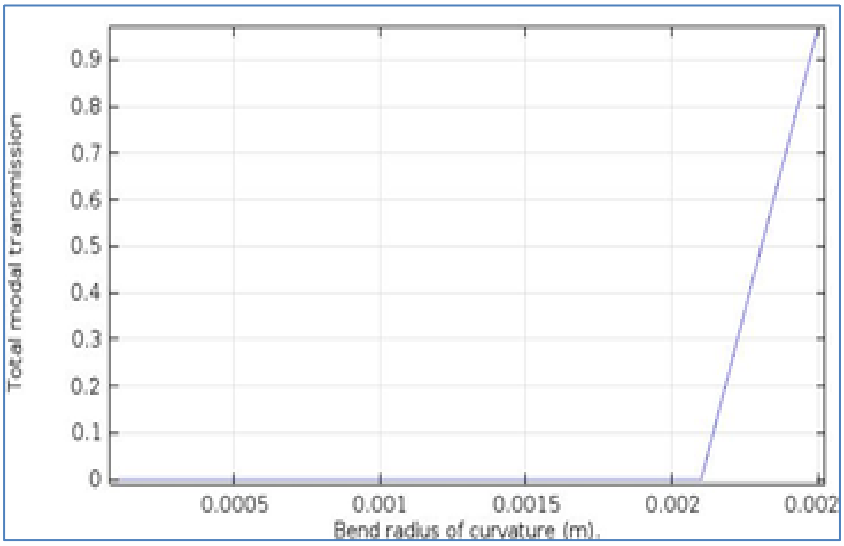

Figure (4.13b): Total transmission versus bend radius of curvature 2.5mm for $LiNbO_3$,the width of wave guide 2.5µm.

B) $SrTiO_3$

Then, compute the relation between the total transmission and bend radius for peroviskite . At the same way using the same parameter and then changing the wave width of the waveguide to find the total transmission and obtain the losses for each state of changing the wave width ,firstly, when the width was (1.5μm)finding the figure of electric field ,that is appear in figure(4.14a)and then find the relation of bend radius as demonstrated figure (4.14b):

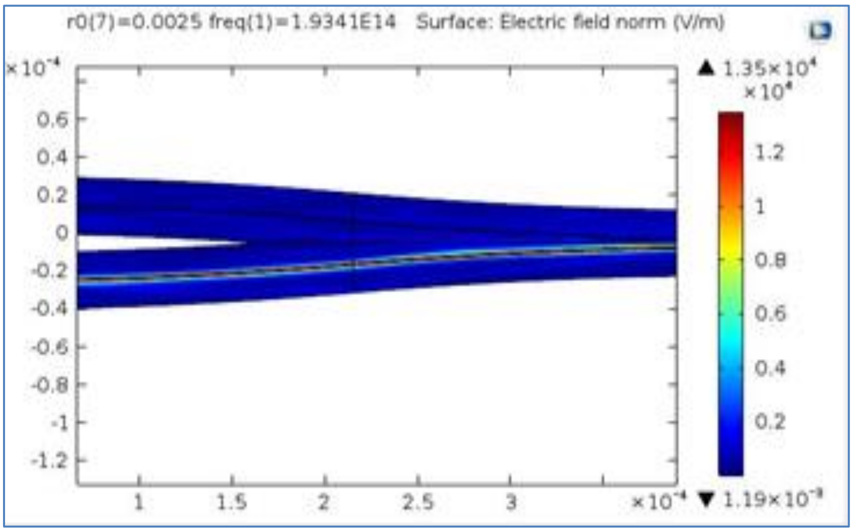

Figure (4.14a):Electric field of the wave guide for two arms of MZM for $SriTO_3$,waveguide width 1.5μm

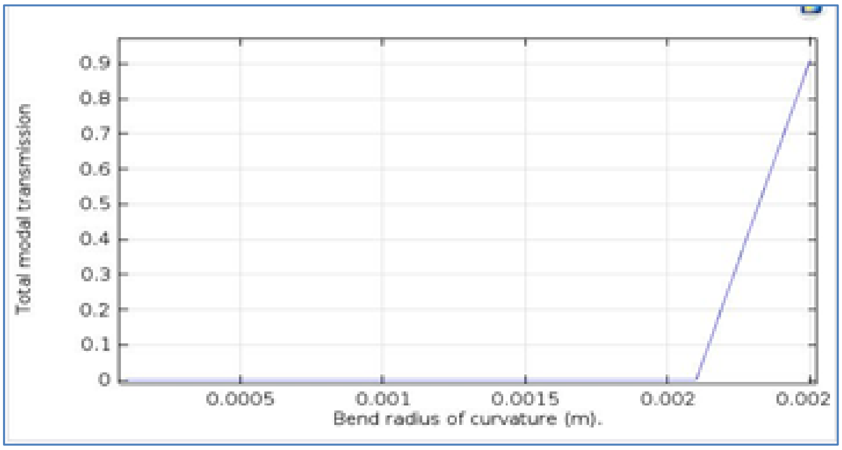

Figure (4.14b): Total transmission versus bend radius of curvature 2.5mm, waveguide width 1.5μm.

When changing the width of the waveguide to (2µm) the result of the total transmission and bend radius shows the losses of this state. That is clear when looking to figure (4.15a) for the electric field and then to figure (4.15b) for the relation :

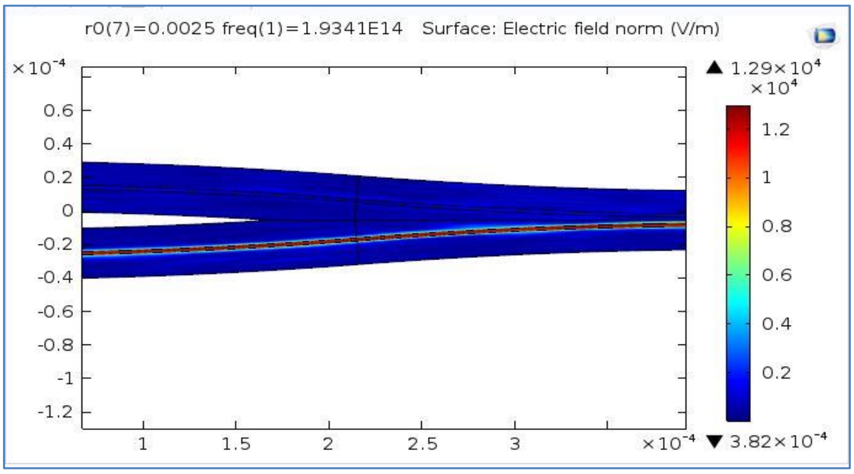

Figure (4.15a): Electric field of the wave guide for two arms of MZM for $SriTO_3$,the waveguide width 2µm.

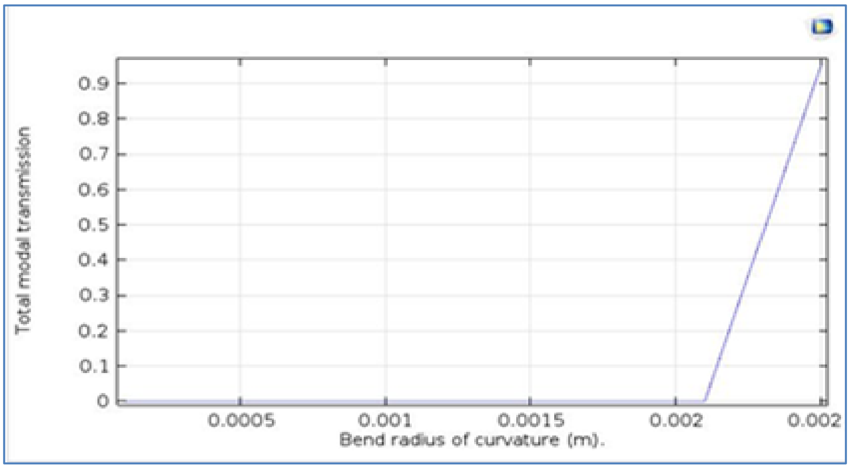

Figure (4.15b): Total modal transmission (y- axis) versus bend radius of curvature 2.5(mm) (x-axis) of MZM based $SriTO_3$.

From the figure (4.15b) the transmission of the material is about 98% and the losses IS approximately 2%, that result is similar to other results for other materials.

C) KNO_3

At last thing same relation for the last materials of this study potassium nitrate at the same way the first state wave width was (1.5µm) that giving transmission approximately 98% of the power . Accept 2% loss and fix the bend radius to be 2.5mm as seen in figure (4.16a ,b):

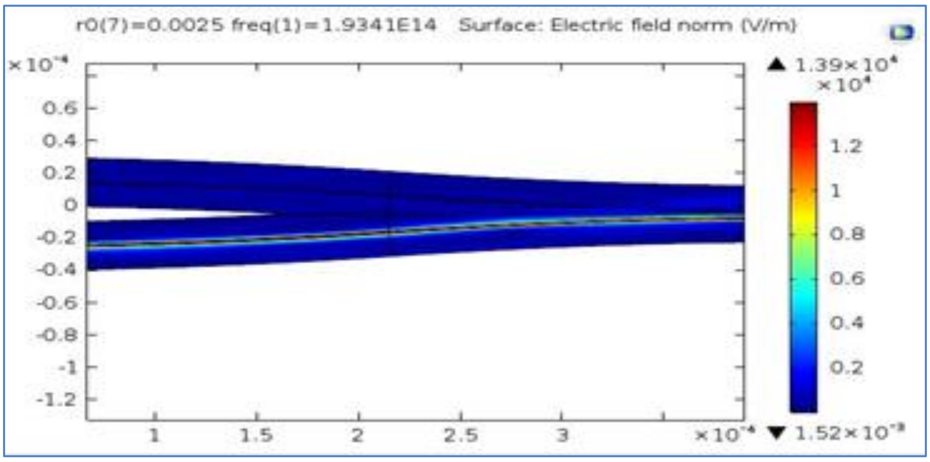

Figure (4.16a):Electric field of the waveguide for two arms of MZM for KNO_3, waveguide width 1.5µm

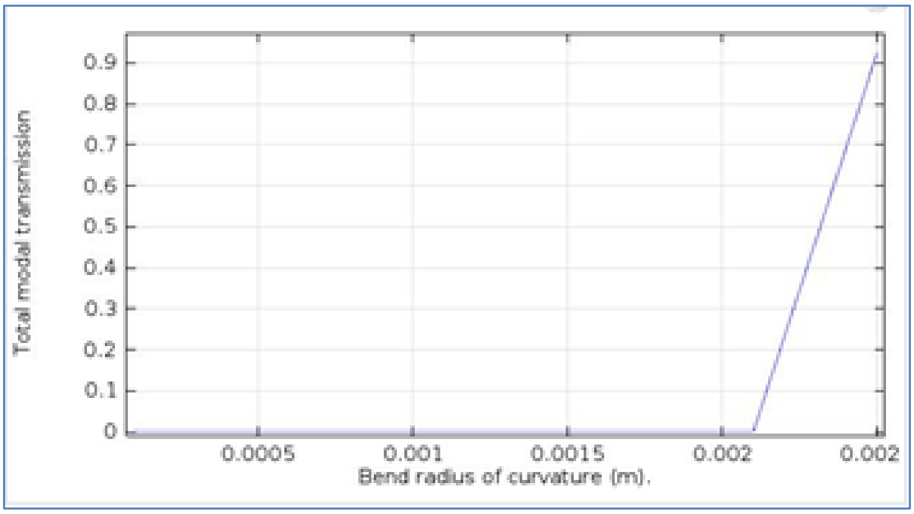

Figure (4.16b): Total transmission versus bend radius of curvature 2.5mm ,the waveguide width 1.5µm.

Later changing the width of the waveguide to (2µm), and find the value of the transmission of the power ,as seen a bend radius of 2.5mm gives a transmission of approximately 98%of the power .just the 2% loss ,and the bend radius still 2.5mm . figure (4.17a,b) explain these statement :

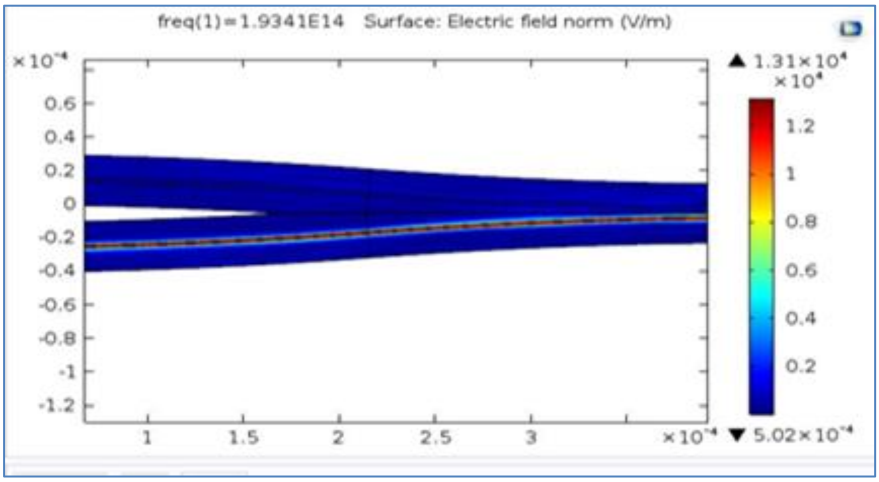

Figure (4.17a):Electric field of MZM based KNO_3.

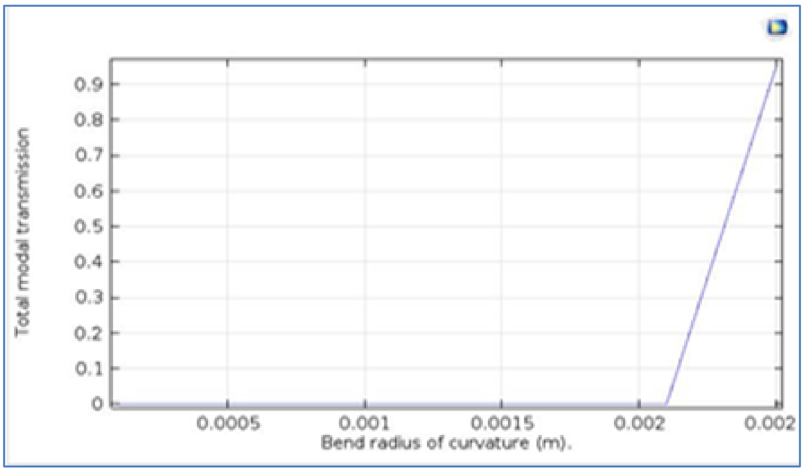

Figure (4.17b): Total modal transmission (y- axis) versus bend radius of curvature 2.5(mm) (x-axis) of MZM based KNO_3.

Then change the wave width to (2.5µm) to see the effect of this changing ,we find the transmission of the power of this state and clearly see the transmission was about 98% and that is seem to another states and the loss about 2% ,that is good result because most of the power transmission and the loss is small value .That is clear in figure (4.18a,b):

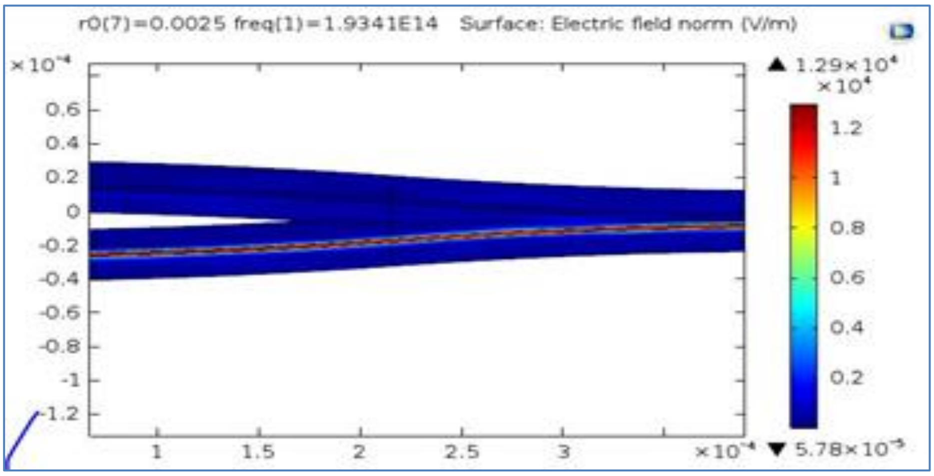

Figure (4.18a):Electric field of the wave guide for two arms of MZM for KNO_3, waveguide width 2.5µm.

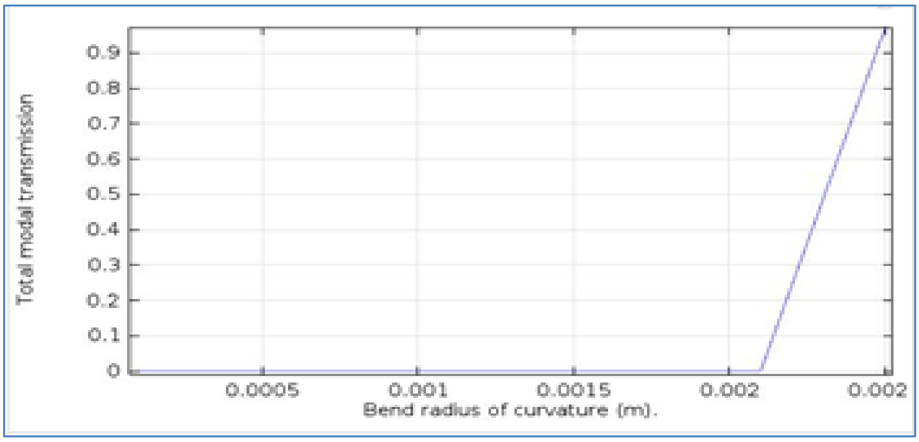

Figure (4.18b): Total transmission versus bend radius of curvature 2.5mm ,the waveguide width 2.5µm

4.2.3 Transmission and Applied Voltage

Finally, a voltage that utilized round the waveguide in one arm (upper) of MZM has analyzed. The voltage supplies will modify the refractive index of the crystals in the arm and that causes a phase difference between the waves propagating through the two arms of MZM. Figure (4.19a,b) showed that the electromagnetic wave can be switch between the two-output waveguide by tuning the applied voltage. In addition, when both input and output ports are connected to other waveguide or fibers the device will works as a spatial switch. However, in case only one input port and one output port are active, the device operates as an amplitude modulator. Figure (4.19a,b) illustrates the relation between the transmission(y-axis) throughout the upper arm (S21) and the lower arm (S41) of MZM waveguide and the electric field for each material versus the applied voltage VO (x-axis). For $LiNbO_3$ (figure 4.20b) the upper line (S21) has maximum output power at (-2.4) and the lower line (S41) has (-12) and both lines crossed approximately at 0.45 V. at the cross point MZ will operate as a modulator. For second material $SriTO_3$, figure (4.23b) shows the upper line with (-2.7) and the lower line with (-9) output power, respectively. Moreover, at approximately 0.38 V there is intersect which represent the point to operate as modulator for MZ. At the end, the last material KNO_3 diagram display the upper line (-2.8) and the lower line (-18) output power, respectively. Traverse between the lines (upper and lower) was at 0.5 V which make MZ operate as modulator.

A) $LiNbO_3$

When we applied the voltage that the wave can be switched between the two output waveguides by tuning the applied voltage. For the first material lithium niobate the first state when the wave width was (1.5 µm)the result was as figure (4.19a,b):

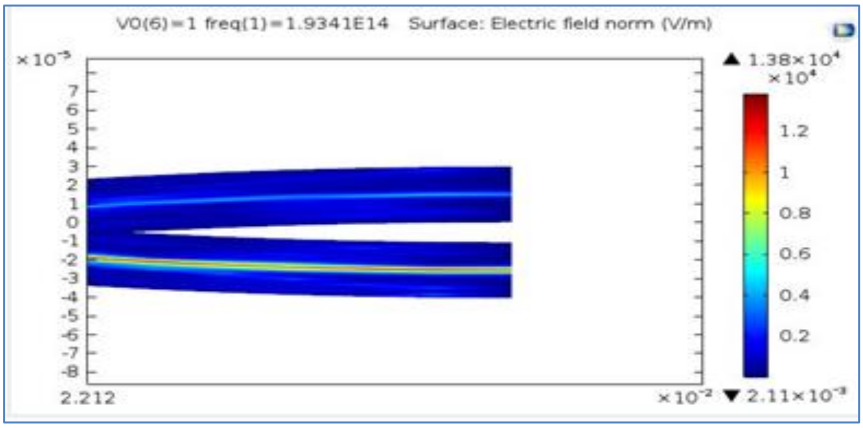

Figure (4.19a):Electric field of the wave of two arms of MZM for $LiNbO_3$, the waveguide width 1.5µm.

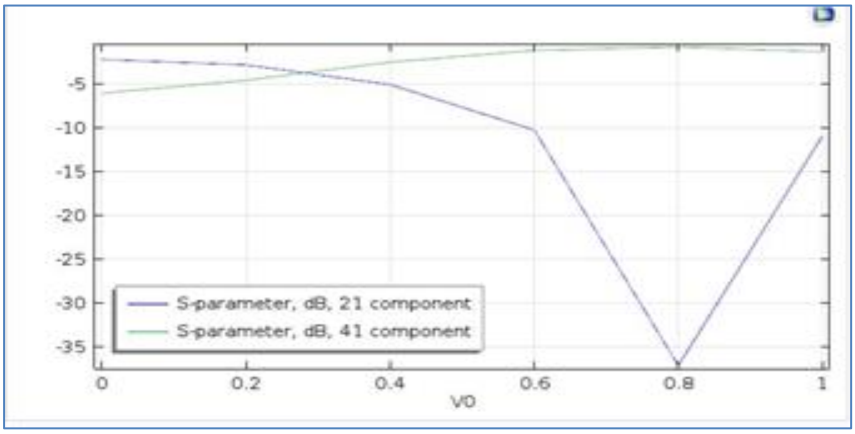

Figure (4.19b): Transmission versus applied voltage Vo, 100volt .the waveguide width 1.5µm.

Then changing the waveguide width to (2µm), the result was changed too as seen in figure (4.20a,b):

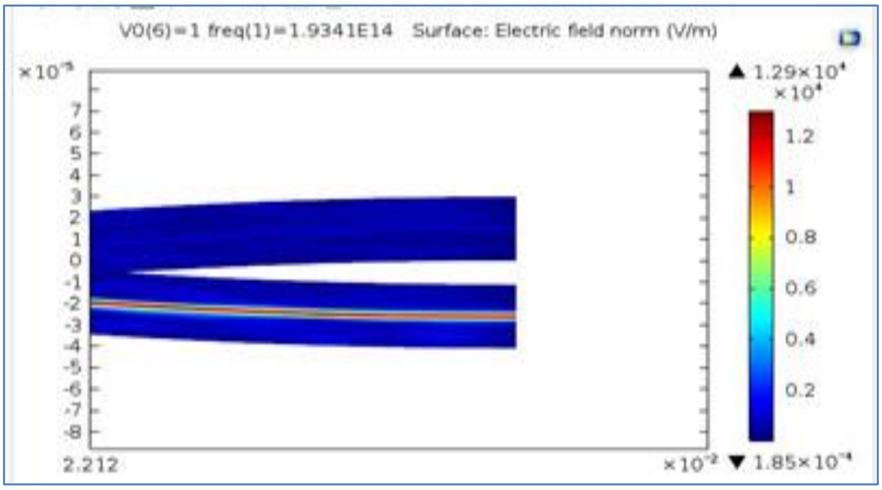

Figure (4.20a):Electric field of MZM based $LiNbO_3$

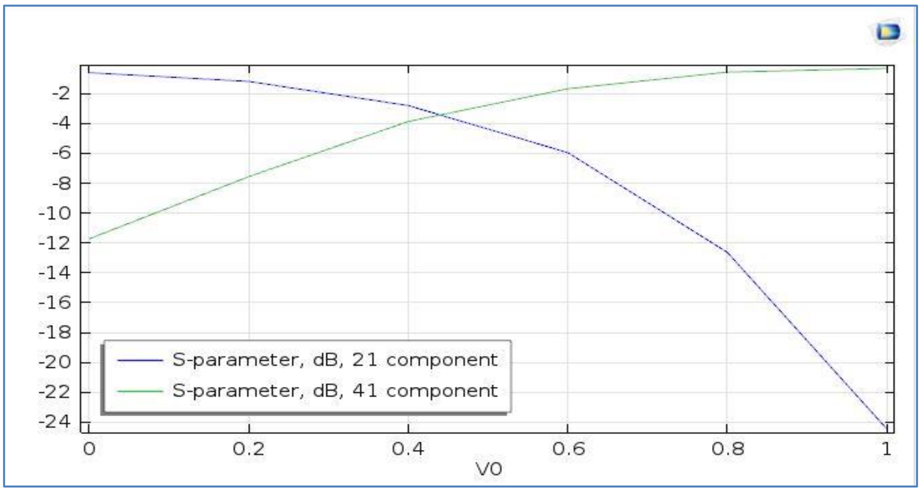

Figure (4.20b): Transmission (output power) (y-axis) to the upper (blue line S21) and lower (green line S41) output power against the applied voltage VO (x-axis) of MZM based $LiNbO_3$.

At the end changing the waveguide width to (2.5μm) and see the result at figure (4.21a,b)

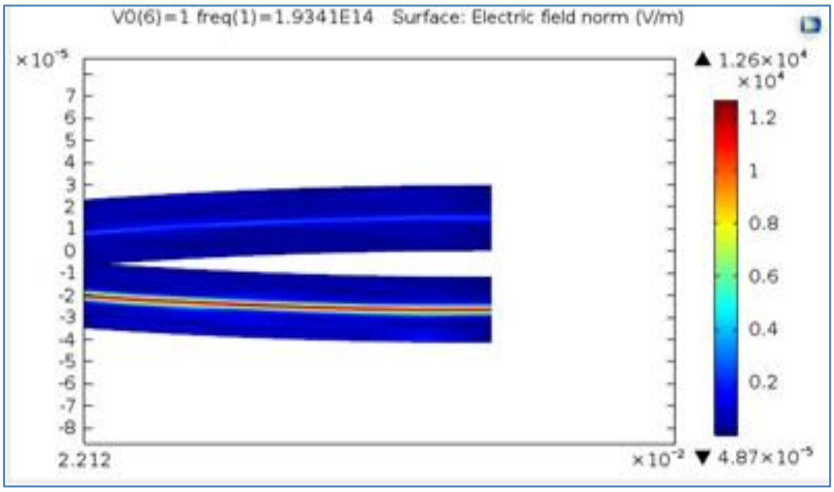

Figure (4.21a):Electric of the wave of two arms of MZM for $LiNbO_3$, the waveguide width 2.5 µm.

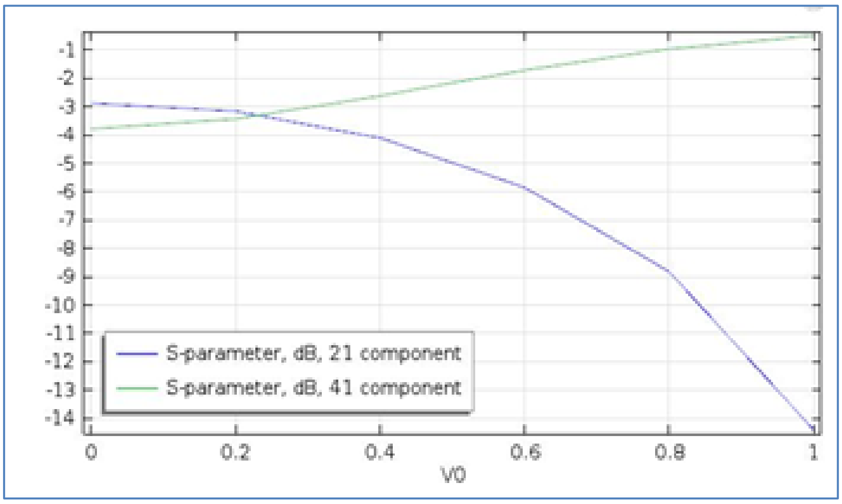

Figure (4.21b): Transmission versus applied voltage Vo, 100volt. The waveguide width 2.5µm.

B) $SrTiO_3$

At the same way repeated the relation of the first material ($LiNbO_3$).Start with the width of the wave(1.5µm)we find the results for perovskite that is clear in figure (4.22a,b):

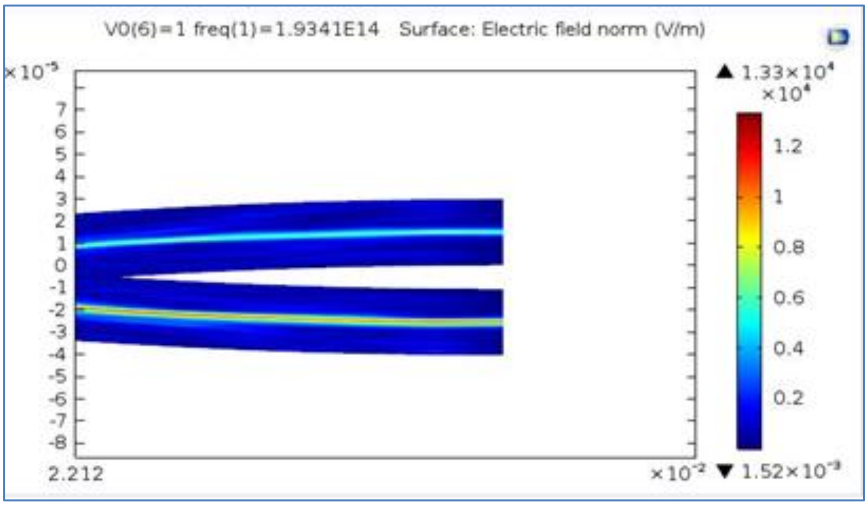

Figure (4.22a):Electric field of the wave of two arms of MZM ,for SriTO3, waveguide width 1.5µm

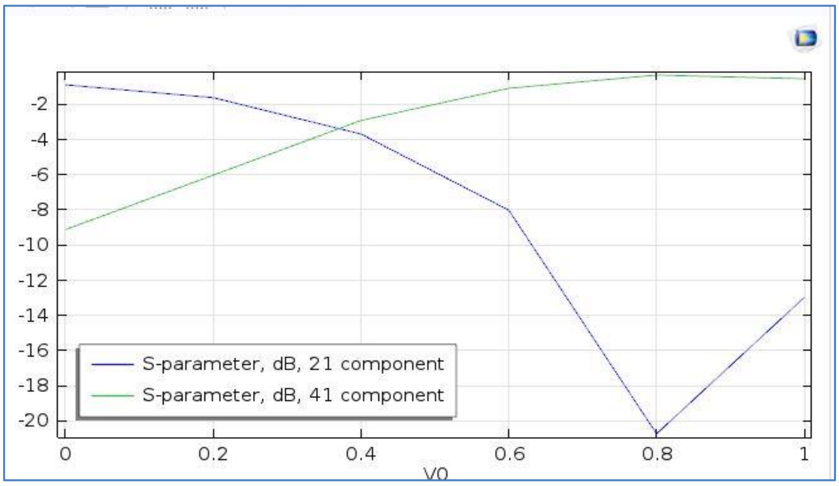

Figure (4.22b): Transmission (output power) (y-axis) to the upper (blue line S21) and lower (green line S41) output power against the applied voltage Vo (x-axis) of MZM based $SrTiO_3$.

And then changing the width of the wave guide to (2µm) the result was change to another value that is appear in figure (4.23a,b):

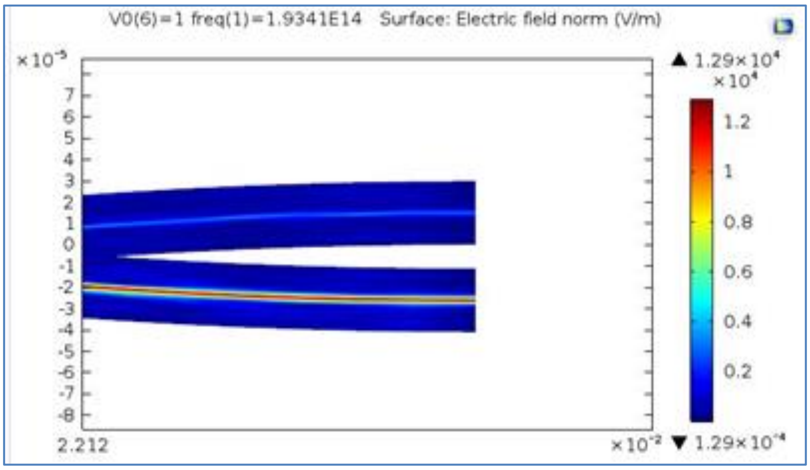

Figure (4.23a): Electric field of the wave of two arms of MZM ,for $SriTO_3$,the waveguide width 2µm.

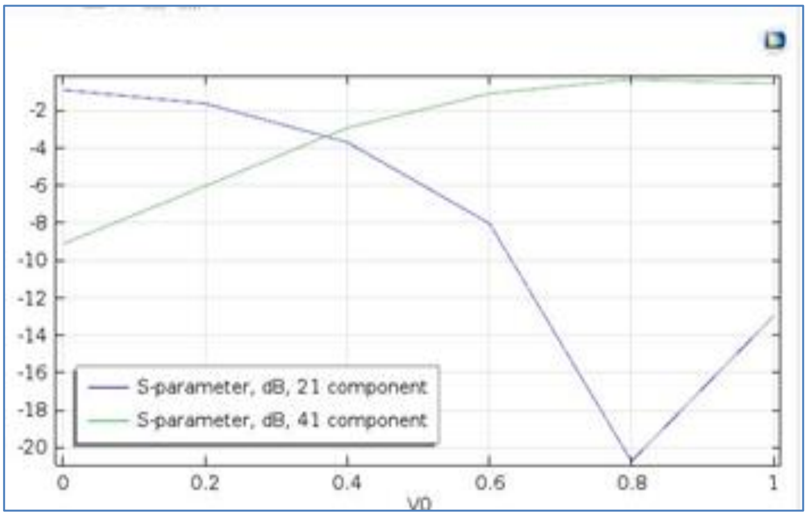

Figure (4.23b): Transmission versus applied voltage Vo, 100 volt,

The wave width 2µm.

Then changing the width of the wave guide to (2.5µm) and then obtain another result other than the previous result ,in this case ,the device does not work as a modulator ,that is clear when see figure (4.24b):

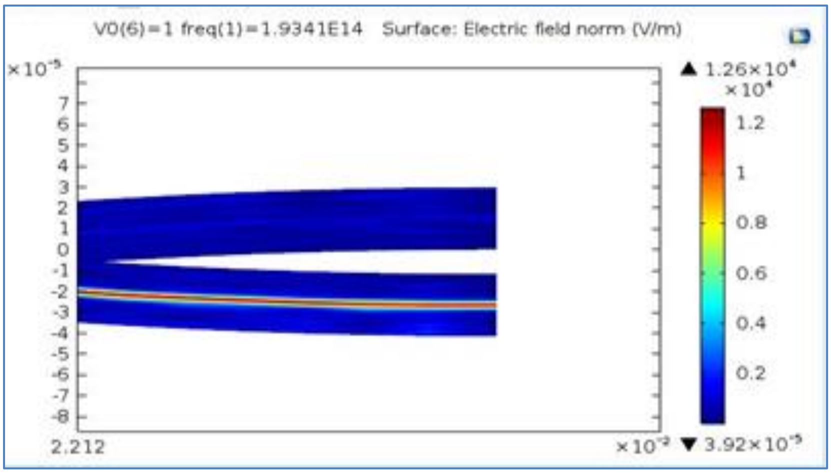

Figure (4.24 a): Electric field of the wave of two arms of MZM, for $SriTO_3$, the waveguide width 2.5μm

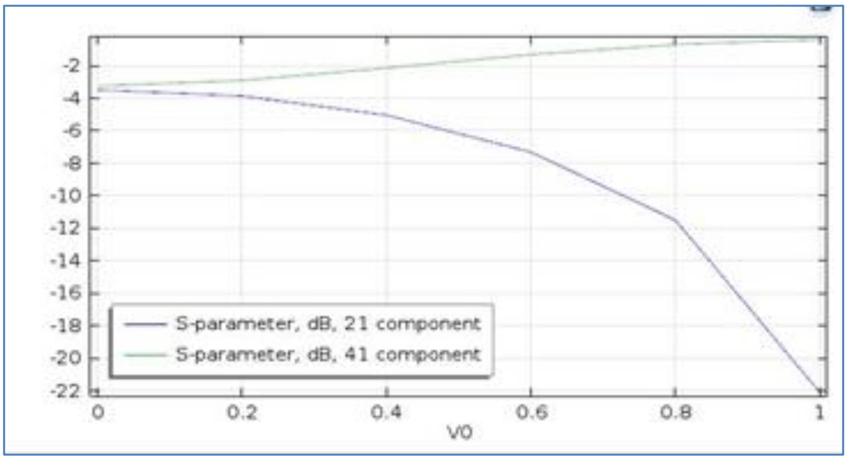

Figure (4.24b): Transmission versus applied voltage Vo, 100 volt , the waveguide width 2.5μm.

The explaining of this case of study beyond to the behavior of the material in terms of work, because the width of the wave was change to (2.5μm). That is mean the previous case was work when the width was (1.52 μm) respectively.

C) KNO_3

Finally, see the results of potassium nitrate from the same structure and parameters of MZM, except the refractive index is different of this material. These results to the same relation, the wave width is changed from (1.5-2-2.5µm) the figures below show the changing:

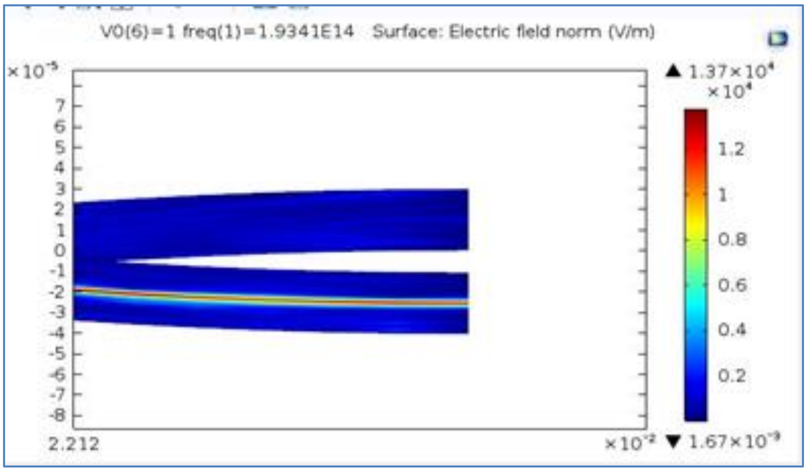

Figure (4.25a):Electric field of the wave guide of two arms of MZM for KNO_3 ,the wave width 1.5µm.

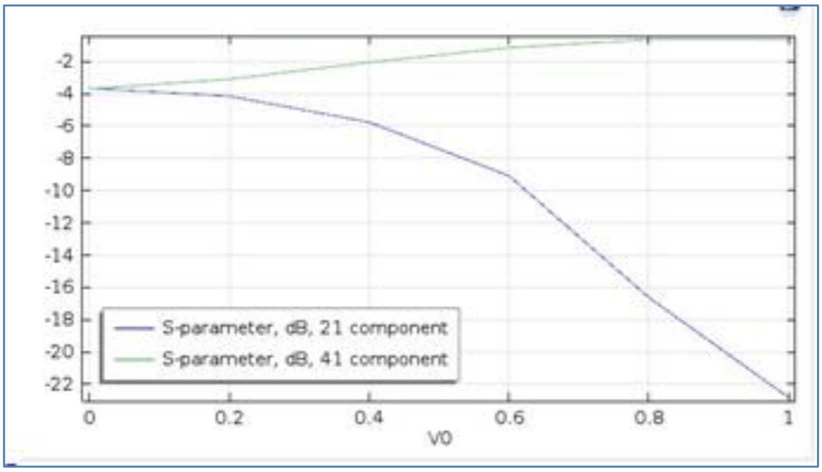

Figure (4.25b): Transmission versus applied voltage Vo,100 volt .the waveguide width 1.5µm.

The first state of this material when the width of the wave was (1.5µm), the devise does not work as a modulator, which is clear when we see the figure (4.25b). when changing the width of the wave , another result appear ,it is different from the previous case .in this case the devise is work as a modulator that is clear when see the figure (4.26 b):

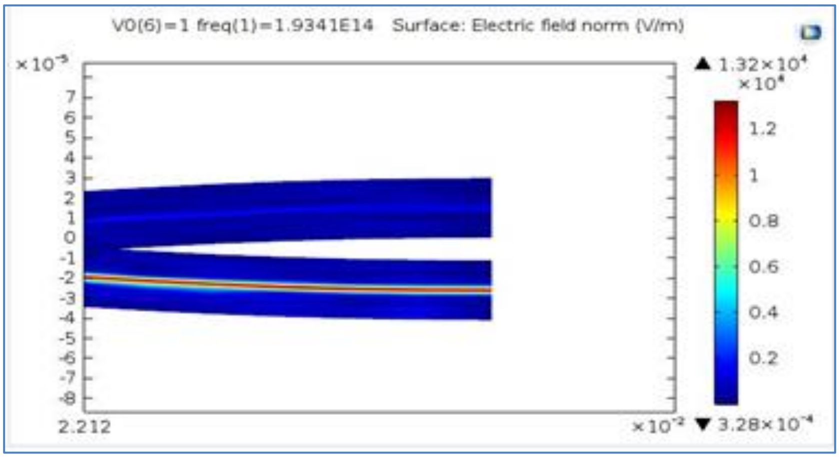

Figure (4.26a):Electric field of the wave guide of two arms of MZM for KNO_3 ,the wave width 2µm

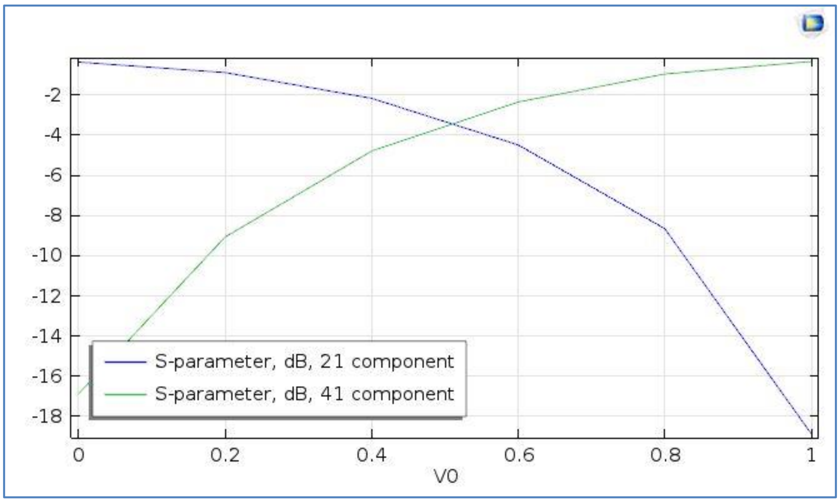

Figure (4.26b): Transmission (output power) (y-axis) to the upper (blue line S21) and lower (green line S41) output power against the applied voltage VO (x-axis) of MZM based KNO_3.

As such in the previous materials and the cases , reaching to the last state when changing the width of the wave guide to (2.5µm) , another result seen that is mean the width of the wave guide can effect of the work of modulator . figure (4.27a,b) can explain these statements when we see these figures .

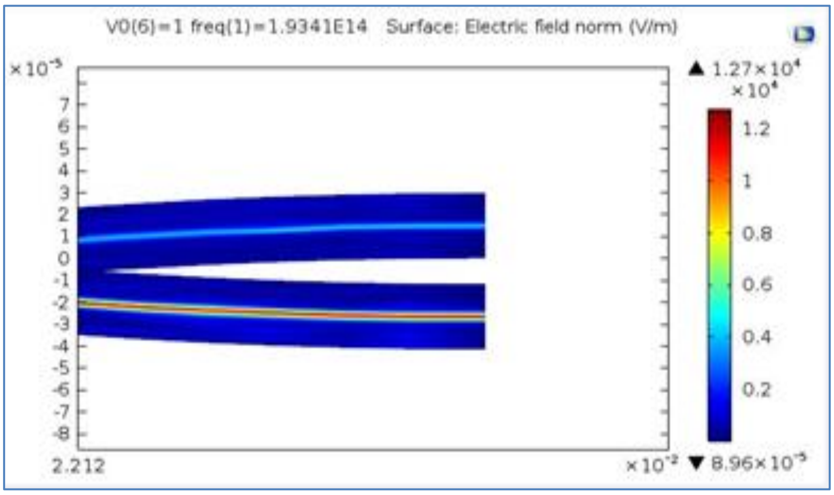

Figure (4.27a):Electric field of the wave guide of two arms of MZM for KNO_3 ,the waveguide width 2.5µm

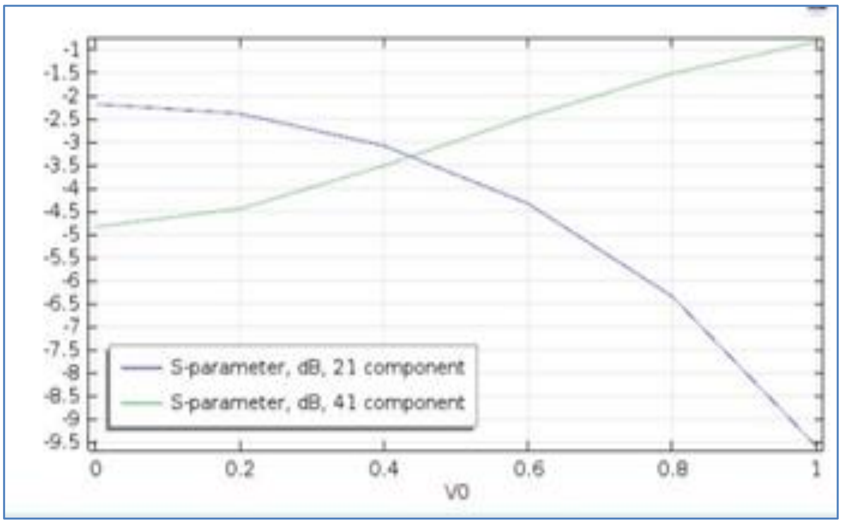

Figure (4.27b): Transmission versus applied voltage .Vo ,100 volt .

Waveguide width 2.5µm.

Chapter Five

Conclusions

and Future Works

5.1 Conclusions

With the rapid advancement of optical technology, electro-optical sensors that detect the electric field in terms of their distinct advantages are rapidly revealing themselves. The electro-optic effect, the intricacies of how the Mach-Zehnder optical modulator works, and the optimum design of its waveguide sensing arm bend radius and length using finite element simulation software COMSOL, followed by a simulation of the applied voltage and the output optical power diagram.

Theoretical and simulation study of MZM based ferroelectric materials by using finite element method is achieved.

1) When the width of the wave guide of (three materials) was (1.5μm) the results were (d-dc =180 μm versus (0.45W/m)of power difference of $LiNbO_3$), while d-dc =240 μm versus 0.55W/m and d-dc =130μm versus 0.35W/m ,for $SrTiO_3$,KNO_3 respectively.
2) When the width of wave guide of three materials was 2μm the results were d-dc = 380 μm versus 0.75W/m of power difference for $LiNbO_3$ while d-dc = 450 μm versus 0.8W/m and d-dc =304 μm versus 0.75W/m for $SrTiO_3$ and KNO_3 respectively.
3) When the width of wave guide was 2.5 μm the results were d-dc =400μm versus 0.9 W/m for $LiNbO_3$, d-dc =405 μm versus 0.85W/m and 450 μm versus 0.95 W/m for $SrTiO_3$ and KNO_3, respectively.
4) The total transmission for three materials are approximately 98%and the losses are 2%, the bend radius is fixed 2.5mm.

5) When the width of waveguide was 1.5μm the relation of transmission and applied voltage, MZM operate as modulator at 0.24V for $LiNbO_3$ while MZM operate at 0.28V, for $SrTiO_3$, but KNO_3 does not work as modulator.
6) When the width of wave guide was 2μm, MZM was operate as modulator at 0.45V, 0.38V and 0.52 V for $LiNbO_3$, $SrTIO_3$, AND KNO_3 respectively.
7) When the width of waveguide was 2.5 μm, MZM work as modulator at 0.22V for $LiNbO_3$, 0.48V for KNO_3 but MZM based $SrTiO_3$ does not work as modulator.
8) By using three different materials, the proposed design has the advantages of flexibility and simplicity in the fabrication.

5.2 Future Works

1) Replace the materials of MZM to another material.
2) Set up voltage at the two arms of MZM and see the effect of this case.
3) Change the length of MZM and see what can be happen to the results.

References:

[1]. Grattan KTV, Sun T. Fiber optic sensor technology: An overview. Sensors Actuators, A Phys. 2000;82(1):40–61.

[2]. Knight JC, Skryabin D V. Nonlinear waveguide optics and photonic crystal fibers. Opt Express. 2007;15(23):15365.

[3]. Address K. Fiber Optic Sensors and Applications. Fiber Opt Sensors Appl. 2020;1–6.

[4]. Carvalho DO, Kassab LRP, Del Cacho VD, da Silva DM, Alayo MI. A review on pedestal waveguides for low loss optical guiding, optical amplifiers and nonlinear optics applications. J Lumin. 2018;203(April):135–144.

[5]. Hill G. The cable and telecommunications professionals' reference: Transport networks. Cable Telecommun Prof Ref Transp Networks. 2012;1–444.

[6]. Grattan KT V, Sun T. Fiber Optic Sensor Technology : An Overview Fiber optic sensor technology : an overview. 2016;4247(November):40–61.

[7]. Kitoh T. ANALYSIS INTRODUCTION TO Solving Maxwell ' s Equations and È dinger Equation the Schro. Vol. 1. 2001.

[8]. Shwetha M, Kumar M, Narayan K. Modeling and simulation of opto-fluidic based Mach-Zehnder interferometer for biosensing application. 2015 Work Recent Adv Photonics, WRAP 2015. 2017;1–4.

[9]. Yin S, Ruffin PB, Yu FTS. Fiber Optic Sensors. CRC Press; 2017. (Optical

Science and Engineering).

[10]. Ahmad M, Hench LL. Effect of taper geometries and launch angle on evanescent wave penetration depth in optical fibers. Biosens Bioelectron. 2005;20(7):1312–1319.

[11]. Messica A, Greenstein A, Katzir A. Theory of fiber-optic, evanescent-wave spectroscopy and sensors. Appl Opt. 1996;35(13):2274.

[12]. Jindal S, Vasishth A, Devi S, Anand G. A review on tungsten bronze ferroelectric ceramics as electrically tunable devices. Integr Ferroelectr. 2018 Jan 2;186(1):1–9.

[13]. Lu H, Bark C-W, Esque de los Ojos D, Alcala J, Eom CB, Catalan G, Gruverman A. Mechanical Writing of Ferroelectric Polarization. Science (80-). 2012 Apr 6;336(6077):59 LP – 61.

[14]. Zhao D, Katsouras I, Asadi K, Groen WA, Blom PWM, De Leeuw DM. Retention of intermediate polarization states in ferroelectric materials enabling memories for multi-bit data storage Dong. Appl Phys Lett. 2016;108(23).

[15]. Chen F, Huang H, Guo L, Zhang Y, Ma T. The Role of Polarization in Photocatalysis. Angew Chemie - Int Ed. 2019;58(30):10061–10073.

[16]. Ludwig Z. Ein neuer Interferenzrefraktor. Zeitschrift für Instrumentenkd. 1891;11:275–285.

[17]. Ahsani V, Ahmed F, Jun MBG, Bradley C. Tapered fiber-optic mach-zehnder

interferometer for ultra-high sensitivity measurement of refractive index. Sensors (Switzerland). 2019;19(7).

[18]. Axelrod D, Burghardt TP, Thompson NL. Total Internal Reflection Fluorescence. Annu Rev Biophys Bioeng. 1984 Jun 1;13(1):247–268.

[19]. Kim MH, Yu BM, Choi WY. A Mach-Zehnder Modulator Bias Controller Based on OMA and Average Power Monitoring. IEEE Photonics Technol Lett. 2017;29(23):2043–2046.

[20]. Khor KN, Shahimin MM. Design of integrated optical Mach-Zehnder interferometer biosensor for ideal surveillance rapid diagnostic test. IECBES 2014, Conf Proc - 2014 IEEE Conf Biomed Eng Sci "Miri, Where Eng Med Biol Humanit Meet." 2014;(December):948–953.

[21]. Burla M, Hoessbacher C, Heni W, Haffner C, Fedoryshyn Y, Werner D, Watanabe T, Massler H, Elder DL, Dalton LR, Leuthold J. 500 GHz plasmonic Mach-Zehnder modulator enabling sub-THz microwave photonics. APL Photonics. 2019;4(5).

[22]. Paloczi GT, Huang Y, Yariv A, Luo J, Jen AK-Y. Replica-molded electro-optic polymer Mach–Zehnder modulator. Appl Phys Lett. 2004;85(10):1662–1664.

[23]. Shukla PK, Sarangpani KK, Talwar S, Purbia GS, Nakhe S V, Vora HS. A modified Mach Zender interferometer for the study of coherence of laser. In: Proc The Education and Training in Optics and Photonics Conference (ETOP), Marseille, France, Oct 23th-27th, 2005. 2005.

[24]. Lee T, Hwang F, Shay W, Lee C. Electromagnetic field sensor using Mach-Zehnder waveguide modulator. Microw Opt Technol Lett. 2006;48(9):1897–1899.

[25]. Kiuchi H, Kawanishi T, Yamada M, Sakamoto T, Tsuchiya M, Amagai J, Izutsu M. High extinction ratio Mach–Zehnder modulator applied to a highly stable optical signal generator. IEEE Trans Microw Theory Tech. 2007;55(9):1964–1972.

[26]. Jarrahi M, Lee TH, Miller DAB. Wideband, low driving voltage traveling-wave Mach–Zehnder modulator for RF photonics. IEEE Photonics Technol Lett. 2008;20(7):517–519.

[27]. Morozov OG, Aybatov DL. Spectrum conversion investigation in lithium niobate Mach-Zehnder modulator. In: Optical Technologies for Telecommunications 2009. International Society for Optics and Photonics; 2010. p. 75230D.

[28]. Watts MR, Zortman WA, Trotter DC, Young RW, Lentine AL. Low-voltage, compact, depletion-mode, silicon MachZehnder modulator. IEEE J Sel Top Quantum Electron. 2010;16(1):159–164.

[29]. Yu Y, Dong J, Li X, Zhang X. UWB monocycle generation and bi-phase modulation based on Mach–Zehnder modulator and semiconductor optical amplifier. IEEE Photonics J. 2011;4(2):327–339.

[30]. Li W, Zhu NH, Wang LX. Reconfigurable instantaneous frequency

measurement system based on dual-parallel Mach–Zehnder modulator. IEEE Photonics J. 2012;4(2):427–436.

[31]. Palmer R, Alloatti L, Korn D, Schindler PC, Baier M, Bolten J, Wahlbrink T, Waldow M, Dinu R, Freude W. Low power Mach–Zehnder modulator in silicon-organic hybrid technology. IEEE Photonics Technol Lett. 2013;25(13):1226–1229.

[32]. Li W, Wang WT, Zhu NH. Photonic generation of radio-frequency waveforms based on dual-parallel Mach–Zehnder modulator. IEEE Photonics J. 2014;6(3):1–8.

[33]. Talataisong W, Wang DN, Chitaree R, Liao CR, Wang C. Fiber in-line Mach–Zehnder interferometer based on an inner air-cavity for high-pressure sensing. Opt Lett. 2015;40(7):1220–1222.

[34]. Huerta-Mascotte E, Sierra-Hernandez JM, Mata-Chavez RI, Jauregui-Vazquez D, Castillo-Guzman A, Estudillo-Ayala JM, Guzman-Chavez AD, Rojas-Laguna R. A core-offset Mach Zehnder interferometer based on a non-zero dispersion-shifted fiber and its torsion sensing application. Sensors. 2016;16(6):856.

[35]. Muwafaq Fadhil J. Optical microfiber-based sensor and pulse fiber laser incorporating graphene saturable absorber/Muwafaq Fadhil Jaddoa. University of Malaya; 2017.

[36]. Tanaka S, Simoyama T, Aoki T, Mori T, Sekiguchi S, Jeong S-H, Usuki T,

Tanaka Y, Morito K. Ultralow-power (1.59 mW/Gbps), 56-Gbps PAM4 operation of Si photonic transmitter integrating segmented PIN Mach–Zehnder modulator and 28-nm CMOS driver. J Light Technol. 2018;36(5):1275–1280.

[37]. Hiraki T, Aihara T, Takeda K, Fujii T, Kakitsuka T, Tsuchizawa T, Fukuda H, Matsuo S. Membrane InGaAsP Mach-Zehnder modulator with SiN: D waveguides on Si platform. Opt Express. 2019;27(13):18612–18619.

[38]. Xie Y, Zhang M, Dai D. Design rule of Mach-Zehnder interferometer sensors for ultra-high sensitivity. Sensors. 2020;20(9):2640.

[39]. Bae Y, Jang S, Yoo S, Yi M, Ryoo J, Shin J. Automatic Bias Control Technique of Dual-Parallel Mach–Zehnder Modulator Based on Simulated Annealing Algorithm for Quadrupled Signal Generation. In: Photonics. Multidisciplinary Digital Publishing Institute; 2021. p. 80.

[40]. Sun Z, Martinez A, Wang F. Optical modulators with 2D layered materials. Nat Photonics. 2016;10(4):227–238.

[41]. Xu Q, Schmidt B, Pradhan S, Lipson M. Micrometre-scale silicon electro-optic modulator. Nature. 2005;435(7040):325–327.

[42]. Nedeljkovic M, Stanković S, Mitchell CJ, Khokhar AZ, Reynolds SA, Thomson DJ, Gardes FY, Littlejohns CG, Reed GT, Mashanovich GZ. Mid-infrared thermo-optic modulators in SoI. IEEE Photonics Technol Lett. 2014;26(13):1352–1355.

[43]. Serhan M, Sprowls M, Jackemeyer D, Long M, Perez ID, Maret W, Tao N,

Forzani E. Total iron measurement in human serum with a smartphone. AIChE Annu Meet Conf Proc. 2019;2019-Novem.

[44]. Williamson LA, Chen YH, Longdell JJ. Magneto-optic modulator with unit quantum efficiency. Phys Rev Lett. 2014;113(20):1–6.

[45]. Nakamura T, Tani S, Ito I, Kobayashi Y. Magneto-optic modulator for high bandwidth cavity length stabilization. Opt Express. 2017;25(5):4994.

[46]. De Lima MM, Beck M, Hey R, Santos P V. Compact Mach-Zehnder acousto-optic modulator. Appl Phys Lett. 2006;89(12):1–4.

[47]. Liu S, Thomson DJ, Li K, Wilson P, Reed GT. N-over-N cascode push-pull modulator driver in 130 nm CMOS enabling 20 Gbit/s optical interconnection with Mach-Zehnder modulator. Electron Lett. 2015;51(23):1900–1902.

[48]. GHATAK AA, Ghatak A, Thyagarajan K, Thyagarajan K. An introduction to fiber optics. Cambridge university press; 1998.

[49]. Winzer PJ, Essiambre RJ. Advanced optical modulation formats. Opt Fiber Telecommun V1B. 2008;94(5):23–93.

[50]. Harris J, Lu P, Larocque H, Chen L, Bao X. In-fiber Mach-Zehnder interferometric refractive index sensors with guided and leaky modes. Sensors Actuators, B Chem. 2015;206:246–251.

[51]. Wong TYK, Freundorfer AP, Beggs BC, Sitch JE, Stage AO. A 10 Gb/s AlGaAs/GaAs HBT High. 1996;31(10):1388–1393.

[52]. Qi N, Li X, Li H, Xiao X, Wang L, Li Z, Gao Z, Yu Y, Miki M, Chiang P. A 25Gb/s, 520mW, 6.4Vpp silicon-photonic mach-zehnder modulator with distributed driver in CMOS. Opt Fiber Commun Conf OFC 2015. 2015;(April):4–7.

[53]. Amin R, Maiti R, Gui Y, Suer C, Miscuglio M, Heidari E, Chen RT, Dalir H, Sorger VJ. Sub-wavelength GHz-fast broadband ITO Mach–Zehnder modulator on silicon photonics. Optica. 2020;7(4):333.

[54]. Xiao J, Tao C, Li J, Zhao Y, Zhang J, Jiang X, Cheng J. Design and modeling of Mach-Zehnder type electro-optic modulators: balanced and unbalanced interferometers. In: ProcSPIE. 2020.

[55]. Bentini GG, Bianconi M, Cerutti A, Chiarini M, Pennestrı G, Sada C, Argiolas N, Bazzan M, Mazzoldi P. Integrated Mach-Zehnder micro-interferometer on LiNbO 3. 2007;45:368–372.

[56]. Zhang QM, Jang SJ, Cross LE. High-frequency strain response in ferroelectrics and its measurement using a modified Mach-Zehnder interferometer. J Appl Phys. 1989;65(7):2807–2813.

[57]. Rizal CS, Niraula B. Compact Si-based asymmetric MZI waveguide on SOI as a thermo-optical switch. Opt Commun. 2018;410(September):947–955.

[58]. Guo S, Albin S. Transmission property and evanescent wave absorption of cladded multimode fiber tapers. Opt Express. 2003;11(3):215.

[59]. Giallorenzi TG, Bucaro JA, Dandridge A, Sigel GH, Cole JH, Rashleigh SC,

Priest RG. Optical Fiber Sensor Technology. IEEE Trans Microw Theory Tech. 1982;30(4):472–511.

[60]. Li L, Xia L, Xie Z, Liu D. All-fiber Mach-Zehnder interferometers for sensing applications. Opt Express. 2012;20(10):11109.

[61]. Setter N, Damjanovic D, Eng L, Fox G, Gevorgian S, Hong S, Kingon A, Kohlstedt H, Park NY, Stephenson GB, Stolitchnov I, Taganstev AK, Taylor D V., Yamada T, Streiffer S. Ferroelectric thin films: Review of materials, properties, and applications. J Appl Phys. 2006;100(5):1–46.

[62]. Iskandar J, Jenie RP, Siregar UJ, Yuliarto B, Irzaman. Application of thin film barium strontium titanate (BST) in a microcontroller based tool to measure oxygen saturation in blood. Ferroelectrics. 2020;554(1):134–143.

[63]. Paillard C, Bai X, Infante IC, Guennou M, Geneste G, Alexe M, Kreisel J, Dkhil B. Photovoltaics with Ferroelectrics: Current Status and Beyond. Adv Mater. 2016;28(26):5153–5168.

[64]. Gao W, Chang L, Ma H, You L, Yin J, Liu J, Liu Z, Wang J, Yuan G. Flexible organic ferroelectric films with a large piezoelectric response. NPG Asia Mater. 2015;7(6).

[65]. Hosono H, Ueda K. Springer Handbook of Electronic and Photonic Materials. Springer Handb Electron Photonic Mater. 2017;1391–1404.

[66]. Owczarek M, Hujsak KA, Ferris DP, Prokofjevs A, Majerz I, Szklarz P, Zhang H, Sarjeant AA, Stern CL, Jakubas R, Hong S, Dravid VP, Stoddart JF. Flexible

ferroelectric organic crystals. 2016;

[67]. Ai Y, Zeng Y, He W, Huang X, Tang Y. Six-Fold Vertices in a Single-Component Organic Ferroelectric wi th Most Equivalent Polarization Directions. 2020;

[68]. Messner A, Eltes F, Ma P, Abel S, Baeuerle B, Josten A, Heni W, Caimi D, Fompeyrine J, Leuthold J. Plasmonic Ferroelectric Modulators. 2019;37(2):281–290.

[69]. Beecroft LL, Ober CK. Nanocomposite Materials for Optical Applications. Chem Mater. 1997;9(6):1302–1317.

[70]. Damjanovic D. Ferroelectric, dielectric and piezoelectric properties of ferroelectric thin films and ceramics. Reports Prog Phys. 1998;61(11):1267–1324.

[71]. Mayergoyz I, Definitions B, Notation AAT, Equations PC. ysteresis in Piezoelectric and Ferroelectric MaterHials. Vol. 3. 2005.

[72]. You YM, Liao WQ, Zhao D, Ye HY, Zhang Y, Zhou Q, Niu X, Wang J, Li PF, Fu DW, Wang Z, Gao S, Yang K, Liu JM, Li J, Yan Y, Xiong RG. An organic-inorganic perovskite ferroelectric with large piezoelectric response. Science (80-). 2017;357(6348):306–309.

[73]. Tang YZ, Gu ZF, Xiong JB, Gao JX, Liu Y, Wang B, Tan YH, Xu Q. Unusual Sequential Reversible Phase Transitions Containing Switchable Dielectric Behaviors in Cyclopentyl Ammonium 18-Crown-6 Perchlorate. Chem Mater.

2016;28(12):4476–4482.

[74]. Courjal N, Porte H, Martinez A, Goedgebuer JP. LiNbO3 Mach-Zehnder modulator with chirp adjusted by ferroelectric domain inversion. IEEE Photonics Technol Lett. 2002;14(11):1509–1511.

[75]. Gupta MC, Ballato J. The handbook of photonics. CRC press; 2018.

[76]. Okayama H. Lithium niobate electro-optic switching. Opt Switch. 2006;39–81.

[77]. Wooten EL, Kissa KM, Yi-Yan A, Murphy EJ, Lafaw DA, Hallemeier PF, Maack D, Attanasio D V, Fritz DJ, McBrien GJ, Bossi DE. A review of lithium niobate modulators for fiber-optic communications systems. IEEE J Sel Top Quantum Electron. 2000;6(1):69–82.

[78]. Heng-Yun Ye1*†, Yuan-Yuan Tang1*, Peng-Fei Li1*, Wei-Qiang Liao1, 2, Ji-Xing Gao1, Xiu-Ni Hua1, Hu Cai2, Ping-Ping Shi1, 3, Yu-Meng You1‡, Ren-Gen Xiong1 2. Metal-free three-dimensional perovskite ferroelectrics. Science (80-). 2018;361(6398):151–155.

[79]. Shi C, Ma JJ, Jiang JY, Hua MM, Xu Q, Yu H, Zhang Y, Ye HY. Large Piezoelectric Response in Hybrid Rare-Earth Double Perovskite Relaxor Ferroelectrics. J Am Chem Soc. 2020;142(21):9634–9641.

[80]. Green MA, Ho-Baillie A, Snaith HJ. The emergence of perovskite solar cells. Nat Photonics. 2014;8(7):506–514.

[81]. Teresa PE, Sornambol M, Gowri S, Aarthi J, Navina M. Growth, spectral,

dielectric, magnetic and antimicrobial studies on dye doped rochelle salt crystal. Results Mater. 2020;6:100095.

[82]. Freney EJ, Garvie LAJ, Groy TL, Buseck PR. Growth and single-crystal refinement of phase-III potassium nitrate, KNO3. Acta Crystallogr Sect B Struct Sci. 2009;65(6):659–663.

[83]. Jia W, Fan C, Wang L, Wang Q, Zhao M, Zhou A, Li J. Extremely Accessible Potassium Nitrate (KNO3) as the Highly Efficient Electrolyte Additive in Lithium Battery. ACS Appl Mater Interfaces. 2016;8(24):15399–15405.

[84]. Yigzaw Y, Gorton L, Akalu G, Solomon T. Fermentation of teff (Eragrostis tef), grass-pea (Lathyrus sativus), and their mixtures: Aspects of nutrition and food safety. Lathyrus Lathyrism Newsl. 2001;2(March):8–10.

[85]. Scott JF, Duiker HM, Beale PD, Pouligny B, Dimmler K, Parris M, Butler D, Eaton S. Properties of ceramic KNO3 thin-film memories. Phys B+C. 1988;150(1–2):160–167.

[86]. Amirov AM, Gafurov MM, Ataev MB, Rabadanov KS. Study of phase composition and structure of KNO3–LiNO3–Al2O3 nanocomposites. Appl Solid State Chem. 2018;2(3):12–16.

[87]. Dong X, Huang L, Liu Q, Zeng H, Lin Z, Xu D, Zou G. Perfect balance harmony in Ba2NO3(OH)3: A beryllium-free nitrate as a UV nonlinear optical material. Chem Commun. 2018;54(45):5792–5795.

[88]. Monk P. Finite element methods for Maxwell's equations. Oxford University

Press; 2003.

[89]. David J. Griffith. INTRODUCTION TO ELECTRODYNAMICS Fourth Edition. 2012.

[90]. Hayt WH, John Buck JA. Engineering Electromechanics. 2001;597.

[91]. Bakshi UA, Bakshi LA V. Electromagnetic field theory. Technical Publications; 2020.

[92]. Wang W. Electromagnetic Wave Theory Refraction and reflection (wave equation). 1986;1–79.

[93]. Kawano K, Kitoh T. Introduction to Optical Waveguide Analysis. Introduction to Optical Waveguide Analysis. Wiley Online Library; 2001.

[94]. Marcuse D. Electrooptic Coupling Between TE and TM Modes in Anisotropic Slabs. IEEE J Quantum Electron. 1975;11(9):759–767.

[95]. Lorrain P, Corson DR, Lorrain F. Electromagnetic Fields and Waves. 1988;

[96]. Xiao J, Tao C, Li J, Zhao Y, Zhang J, Jiang X, Cheng J, Devices O, Only O. Design and modeling of Mach- Zehnder type electro-optic modulators: balanced and unbalanced interferometers. 2021;(October 2020).

[97]. Shi YF, Liu J. Multi-Physics Modeling and Simulation of Electro-Optical Sensing. Adv Mater Res. 2015;1092–1093:292–295.

[98]. Chen Q, Konrad A. A review of finite element open boundary techniques for

static and quasi-static electromagnetic field problems. IEEE Trans Magn. 1997;33(1 PART 2):663–676.

[99]. Felippa CA. Introduction to finite element methods. Univ Color. 2004;885.

[100]. Zieli TG. Introduction to the finite element method. 1992;

[101]. Aldawsari S. Nonlinear Hybrid Plasmonic Waveguides. 2013;

[102]. Das AK, Chatterjee S. Finite element method-based modelling of flow rate and temperature distribution in an oil-filled disc-type winding transformer using COMSOL multiphysics. IET Electr Power Appl. 2017;11(4):664–673.

[103]. Schreiber B, Elsayad K, Heinze KG. Axicon-based Bessel beams for flat-field illumination in total internal reflection fluorescence microscopy. Opt Lett. 2017;42(19):3880–3883.

[104]. Axelrod D. Total Internal Reflection Fluorescence Microscopy in Cell Biology. 2001;(2):764–774.

[105]. Burghardt TP, Francisco S. Total Internal. Cardiovasc Res. 1984;(17):247–268.

[106]. Zou Y, Chakravarty S, Chung C-J, Xu X, Chen RT. Mid-infrared silicon photonic waveguides and devices [Invited]. Photonics Res. 2018;6(4):254–276.

الخلاصة

تستخدم المضمنات الكهروضوئية المعتمدة على الدليل الموجي على نطاق واسع في مجال الاتصال البصري، معالجة الإشارات الضوئية وأجهزة الاستشعار البصرية بفضل التطور السريع للدوائر المتكاملة الضوئية. كنوع من عناصر التحويل البصري، يعد مُضمن ماك-زيندر أحد أكثر مكونات الأجهزة استخدامًا ،مع مزايا الدقة العالية والحساسية. من خلال البحث النظري والعددي تم دراسة ثلاثة أنواع من مُضمنات ماك-زندر على أساس المواد الفيروكهربائية وهي نيوبات الليثيوم و البيروفيسكايت ونترات البوتاسيوم. خصائص الإرسال لمضمن ماك-زندر تم تحليلها عدديًا أثناء تطبيق مجال كهربائي عبر احد اذرع الدليل موجي. المضمن ماك-زندر المعتمد على المواد الفيروكهربائية درس نظريًا ونمذج باستخدام طريقة العناصر المحدودة مع برنامج COMSOL Multiphysics. تم تجربة معاملات مختلفة لـ MZM وهي طول الاقتران ونصف قطر الانحناء والجهد المطبق. أظهرت النتائج أن أقل طول اقتران لـ MZM كان 304 ميكرومتر باستخدام بلورات نترات البوتاسيوم. يعمل ماك-زندر كمضمن عند نصف قطر للانحناء بمقدار 2.5 مم لجميع البلورات الفيروكهربية الثلاثة ولم يعمل مع نصف قطر أقل من هذا . أظهر تأثير الجهد المستخدم أن مضمن ماك-زندر يعمل بفعالية عند 0.38 فولت باستخدام البيروفسكايت. بينما كان الجهد الفعال لكل من ليثيوم نيوبيت 0.45 فولت ونترات البوتاسيوم 0.5 فولت على التوالي. كان فقد الطاقة لجميع عينات ماك-زندر %2 .

وزارة التعليم العالي والبحث العلمي

جامعة المثنى كلية العلوم

قسم الفيزياء

نمذجة الالياف البصرية المايكروية (ماك –زندر الخطي) في تطبيقات التحسس.

رسالة مقدمة كجزء من متطلبات نيل شهادة الماجستير في علوم الفيزياء

من قبل الطالبة

حنان جاسم محمد

بكلوريوس علوم فيزياء ٢٠٠٣

بإشراف

ا.م.د فراس فائق كاظم　　　　ا.م.د موفق فاضل جدوع

٢٠٢١ م　　　　١٤٤٣هـ